KLOE Note 212
August 2006

Study of the $e^+e^- \to \pi^0\pi^0\gamma$ process using 2001/2002 data

S. Giovannella, S. Miscetti

INFN - Laboratori Nazionali di Frascati

Abstract

In this note, we report the measurement of the visible cross section for the $\pi^0\pi^0\gamma$ final state performed using 450 pb^{-1} of e^+e^- collisions collected in the 2001−2002 data taking period. The separation between $e^+e^- \to \omega\pi^0 \to \pi^0\pi^0\gamma$ and $\phi \to \pi^0\pi^0\gamma$ processes is done in the hypothesis of no interference. Under this assumption, we study the dependence of the cross sections on the center of mass energy in the range 1017.0−1022.0 MeV and fit them to extract the relevant parameters of the $e^+e^- \to \omega\pi^0$ process and the branching fraction for the process $\phi \to \pi^0\pi^0\gamma$, dominated by a scalar meson exchange in the intermediate state. We determine BR$(\phi \to \pi^0\pi^0\gamma) = (\,1.057 \pm 0.046_{\rm fit} \pm 0.017_{\rm norm}\,) \cdot 10^{-4}$, still consistent with our previous measurement.

1 Introduction

The interest in light scalar mesons is still alive in hadron spectroscopy, due to the possibility of having found exotic particles. Indeed, there are several models to describe their nature, like ordinary $q\overline{q}$ meson, $q\overline{q}q\overline{q}$ state, $K\overline{K}$ molecule [1, 2, 3].

The KLOE experiment is well suited to study these particles, since the radiative decays of the ϕ in two pseudoscalar mesons is dominated by scalar meson exchange in the intermediate state ($\phi \to S\gamma \to \pi\pi\gamma/\eta\pi\gamma$). Considering the $\pi^0\pi^0\gamma$ final state, the possible contributions come from the well established $f_0(980)$ and the more controversial $\sigma(600)$, which was recently seen by the E791 and BES collaborations [4, 5]. There is also a non-resonant reaction that contributes to the same final state: the $e^+e^- \to \omega\pi^0 \to \pi^0\pi^0\gamma$ process.

The $\pi^0\pi^0\gamma$ final state was already studied at KLOE using 16 pb^{-1} of 2000 data [6, 7]. The high value of the BR favours the $q\overline{q}q\overline{q}$ composition of the $f_0(980)$ while the fit to the $\pi^0\pi^0$ invariant mass suggests a possible contribution also from the $\sigma(600)$. In this note we analyze a sample which is almost thirty times higher in statistics, which allows to study more deeply the mass spectra. Moreover, data were taken at different values of the center of mass energy, $\sqrt{s}$, giving the possibility to study the behaviour of the visible cross sections as a function of $\sqrt{s}$. Differently from the past, we have developed a single set of cuts and algorithms for the resonant and not-resonant processes. This will allow the extraction of the two components by directly fitting the Dalitz plot of the $\pi^0\pi^0\gamma$ final state. This will be discussed in a forthcoming note [8].

2 Signal and backgrounds

To better explain the contributions to the $\pi^0\pi^0\gamma$ final state we show in Fig. 1 the Dalitz plot of $M_{\pi\gamma}$ *vs* $M_{\pi\pi}$, where we enter twice per event (${\pi^0}_1\gamma$, ${\pi^0}_2\gamma$). There are two processes that contributes at the center of mass energy around the ϕ mass (M_ϕ):

1. $e^+e^- \to \omega\pi^0 \to \pi^0\pi^0\gamma$ ($\omega\pi$)
   This process is concentrated in the two narrow bands that are clearly visible in the $\pi^0\pi^0\gamma$ Dalitz plot. The visible cross section at the ϕ mass is $\sigma_{\omega\pi}(M_\phi) \sim 0.5$ nb, and the behaviour as a function of $\sqrt{s}$ is linear, with a dip around M_ϕ due to the interference with the $\phi \to \omega\pi^0$ decay [9].

2. $\phi \to S\gamma \to \pi^0\pi^0\gamma$ ($S\gamma$)
   These events populates mainly the high $M^2_{\pi\pi}$ region of the Dalitz plot, with a visible cross section of $\sigma_{S\gamma}(M_\phi) \sim 0.3$ nb.

The background channels for the $\pi^0\pi^0\gamma$ final state are listed in Tab. 1, together with the corresponding signal ($S\gamma + \omega\pi$) over background ratio. It can be noted that only the $\phi \to a_0\gamma$ channel ($\eta\pi\gamma$) has the same five photon final state. The $\phi \to \eta\gamma \to \pi^0\pi^0\pi^0\gamma$ ($\eta\gamma_7$) mimics the signal because of lost or merged photons while the three photon final states ($\phi \to \eta\gamma$ [$\eta\gamma_3$], $\phi \to \pi^0\gamma$ [$\pi\gamma$] and $e^+e^- \to \gamma\gamma(\gamma)$ [$\gamma\gamma$]) produces five clusters due to splitting or accidental coincidence with clusters produced by machine background. The low signal over background ratio (S/B) value for these last channels make them anyhow a relevant contribution to the background.

Process	S/B
$\phi \to a_0\gamma \to \eta\pi^0\gamma \to \gamma\gamma\pi^0\gamma$	8.51
$\phi \to \eta\gamma \to \pi^0\pi^0\pi^0\gamma$	0.06
$\phi \to \eta\gamma \to \gamma\gamma\gamma$	0.06
$\phi \to \pi^0\gamma$	0.21
$e^+e^- \to \gamma\gamma(\gamma)$	0.002

Table 1: Signal over background ratio for the main background channels of the $\pi^0\pi^0\gamma$ final state.

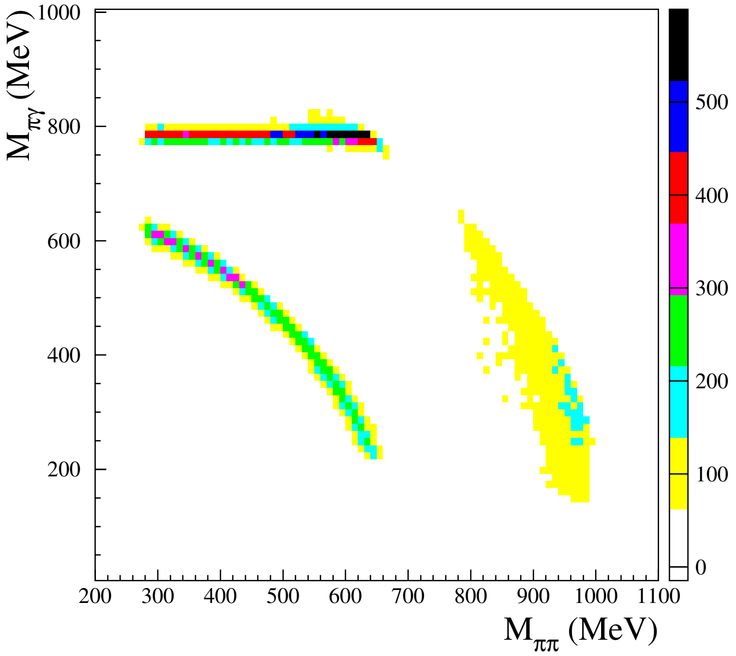

Figure 1: Dalitz plot for the $\pi^0\pi^0\gamma$ final state. The two bands on the left correspond to the $e^+e^- \to \omega\pi^0 \to \pi^0\pi^0\gamma$ process while the region with $M_{\pi\pi} > 700$ MeV is dominated by the $\phi \to S\gamma \to \pi^0\pi^0\gamma$ decay.

3 Data and Montecarlo samples

In this analysis, we have used all the available statistics collected in 2001−2002 data-taking periods which corresponds to 450 pb^{-1}. The two data-taking periods have a substantial difference on the rate of machine background, *dafbkg*, however this influences only at the % level the evaluation of the signal efficiency while impacts in the background evaluation only for the calibration of the $\eta\gamma_3$, $\pi\gamma$ and $\gamma\gamma$ decays. A slightly reduced but cleaner data sample has been obtained after applying a data quality procedure which is described in detail in the next subsection. The data analysis was done using the neutral radiative DST stream, called *drn*, produced with the datarec versions 13 and 14.

As described in Ref. [11], for each run ($L_{\rm int} \sim 200$ nb^{-1}) the large angle Bhabha events are used to estimate both the luminosity and the beam parameters (beam position, ϕ boost, $\sqrt{s}$...). The most relevant parameter to classify our sample is the center of mass energy, which varies of ± 1 MeV around the ϕ mass, as shown in Fig. 2. Moreover, we had a low statistics energy scan in 2001 while at the end of 2002 two dedicated off-peak runs at 1017 and 1022 MeV have been also acquired. Since we know $\sqrt{s}$ with a relative precision of 30 keV for a typical run of ~ 200 pb^{-1}, we have grouped all events in bins of 100 keV. Only bins with an integrated luminosity of at least 1 pb^{-1} have been considered. The absolute calibration of the center of mass energy has been performed by fitting the data of the ϕ-scan to extract the ϕ mass [12]. A careful comparison with the ϕ mass evaluated by SND with the depolarization method translates in an absolute energy shift of 150 keV. This correction has been applied when classifying our sample.

For the Montecarlo (MC) samples we use the DSTs of the official 2001/2002 KLOE production for the neutral radiative stream, RAD04 and GG04, whose integrated luminosity is five times the collected data for all the signal and backgrounds, excepted the $\gamma\gamma$ events that are produced at 1:1 rate. All the MC was produced and reconstructed with the datarec version 18, which has many improvements with respect to our old analysis. From the calorimeter point of view, the photon properties on the simulation (resolutions and detection efficiency) have been tuned with data using a large sample of γ tagged in $\phi \to \pi^+\pi^-\pi^0$ events selected by drift chamber information only [11]. The presence of additional clusters in the events due to accidental overlap with machine background clusters has been taken care of by inserting these events at hit level in the simulation. The *dafbkg* was inserted with the idea to follow its rate dependence along the running period [11].

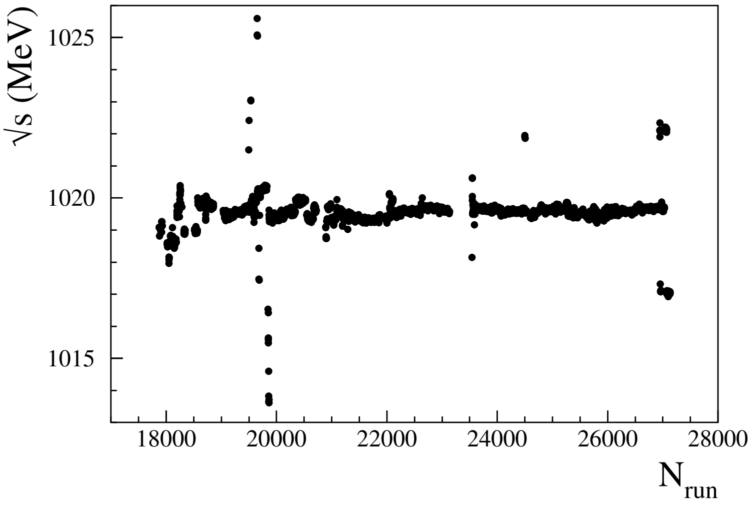

Figure 2: Center of mass energy as a function of the run number. The two energy scans of 2001 ($N_{run} \approx 19700$) and 2002 ($N_{run} \approx 27000$) data are clearly visible.

A software bug was discovered in this procedure; the calibration of the accidental rate has been done looking at out-of-time events and is described in [13]. Similarly, all the other basic running conditions, such as beam parameters ($\sqrt{s}$, ϕ boost, beam position) follow the run variation. Another important improvement is the description of the MC generators for both the signal processes, as discussed in Par. 3.2.

3.1 Data quality and sample classification

The reconstructed data of 2001/2002 have been cleaned up further on by removing runs with some missing beam parameter, not standard calorimeter thresholds as reported in Ref. [14], or an anomalous event counting for the $\phi \to \eta\gamma \to \pi^0\pi^0\pi^0\gamma$ decay, indicating a failure in the chain of the data reconstruction and streaming. This decay has been chosen because it is the most abundant of the drn stream and it is practically background free. The selection criteria is very simple, following the recipe of [15]: seven neutral clusters in angular acceptance ($23° < \theta_\gamma < 157°$), with at least one photon with energy greater than 280 MeV. The luminosity measurement obtained using the Very Large Angle Bhabha

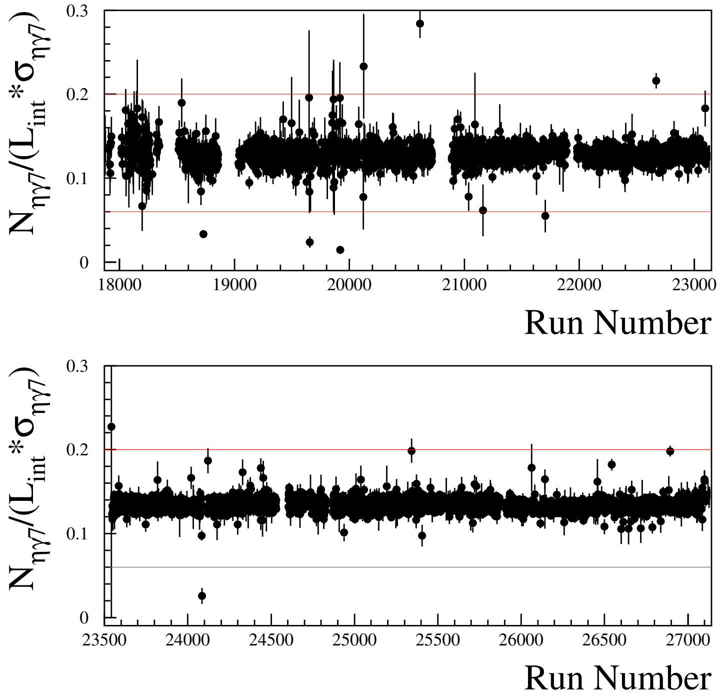

Figure 3: Number of events $\phi \to \eta\gamma$ with $\eta \to \pi^0\pi^0\pi^0$ as a function of the run number, normalized to product of the integrated luminosity and the $\phi \to \eta\gamma$ visible cross section. Top and bottom histograms represent 2001 and 2002 data respectively.

(VLAB) sample [16], $L_{\rm int}$, and the $\phi \to \eta\gamma$ visible cross section as a function of $\sqrt{s}$ from the 2002 scan [17], $\sigma_{\eta\gamma7}$, are used to normalize the number of events ($N_{\eta\gamma7}$). In Fig. 3 this quantity is reported for each run number. The central value is in good agreement with the expected value: $N_{\eta\gamma7}/(L_{\rm int} \cdot \sigma_{\eta\gamma7}) = \varepsilon_{\rm ana} \cdot {\rm BR}(\eta \to \pi^0\pi^0\pi^0) = 0.41 \cdot 0.325 = 0.13$. The evaluation of the analysis efficiency $\varepsilon_{\rm ana}$ and $\sigma_{\eta\gamma7}$ are reported in more detail in App. A.

Runs with pathological behaviour are removed from the data set. A confidence interval of 0.13 ± 0.07, delimited by the red lines of Fig. 3, is chosen to accept them for the analysis. The list of the discarded runs is given in Tab. 2. The corresponding total luminosity is small, around 1.3 pb^{-1}. The integrated luminosity for each $\sqrt{s}$ value after removing these runs is reported in Tab. 3.

Run Number	Reason
18730	Bad $N_{\eta\gamma7}$ counting
19654	Bad $N_{\eta\gamma7}$ counting
19920	Bad $N_{\eta\gamma7}$ counting
20613	Bad $N_{\eta\gamma7}$ counting
22667	Bad $N_{\eta\gamma7}$ counting
23103–23113	$\sqrt{s}$, p_x missing
23988	Non-standard EMC thresholds
24085	Bad $N_{\eta\gamma7}$ counting
26080	Non-standard EMC thresholds
26883	$\sqrt{s}$, p_x missing
27083	$\sqrt{s}$, p_x missing
27137	$\sqrt{s}$, p_x missing

Table 2: List of runs excluded from the analysis. The corresponding luminosity is 1.3 pb^{-1}.

3.2 Improvements on the MC generators

In the RAD04 production a lot of improvements in the MC generators were done for the scalar meson studies. First of all, the mass spectra for the $f_0(980)$ and $a_0(980)$ are produced according to the shapes obtained from 2000 data [18].

Another important point is the development of a new $e^+e^- \to \omega\pi^0 \to \pi^0\pi^0\gamma$ generator. In the past this process was treated as a chain of two body decays. A large discrepancy was observed in the data-MC comparison [6]. The new generator is instead based on the Vector Meson Dominance (VMD) description of the three body decay according to [9]. An hit-or-miss procedure is then applied to correctly reproduce the $\Delta\phi$ angular distribution.[1] Six different diagrams contribute to this generator, as summarized in Fig. 4. Possible contributions from the ρ' (see [9]) are not considered.

In order to check if the new generator was improving the data-MC agreement, we have applied the old analysis to the new data sets. In Figs. 5, 6 the data-MC comparison shows

[1]This variable is defined as $\Delta\phi = \phi'_\gamma - \phi_\omega$. ϕ_ω is the ω azimuthal angle in the laboratory rest frame (LRF), while ϕ'_γ is the γ azimuthal angle in the helicity rest frame (HRF). HRF is defined as the ω rest frame with the z coordinate oriented along the ω direction in LRF.

Nominal $\sqrt{s}$ (MeV)	Corrected $\sqrt{s}$ (MeV)	Luminosity (pb^{-1})
1017.0	1017.15	4.05 ± 0.02
1017.1	1017.25	3.45 ± 0.02
1019.2	1019.35	1.39 ± 0.01
1019.3	1019.45	26.70 ± 0.13
1019.4	1019.55	42.13 ± 0.21
1019.5	1019.65	77.49 ± 0.39
1019.6	1019.75	145.01 ± 0.73
1019.7	1019.85	100.35 ± 0.55
1019.8	1019.95	15.16 ± 0.08
1019.9	1020.05	7.68 ± 0.04
1020.0	1020.15	3.01 ± 0.02
1020.3	1020.45	2.89 ± 0.01
1022.1	1022.25	4.23 ± 0.02
1022.2	1022.35	1.70 ± 0.01

Table 3: Integrated luminosity for the different center of mass energies. The nominal value of $\sqrt{s}$ has been shifted to take into account the ϕ mass calibration. Only $\sqrt{s}$ values with $L_{\rm int} > 1$ pb^{-1} are considered.

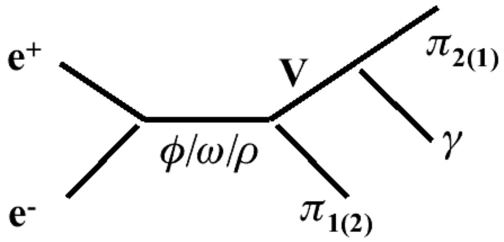

Figure 4: VMD diagrams contributing to the $\pi^0\pi^0\gamma$ final state. V is a vector meson: ϕ, ρ or ω.

a much better description of data than in the past. In particular, the disagreement on the $\cos\psi$ [2] variable is disappeared, while the energy spectra of the π^0 and γ produced in the

[2] ψ is the angle between the γ and the π^0 in the $\pi^0\pi^0$ rest frame.

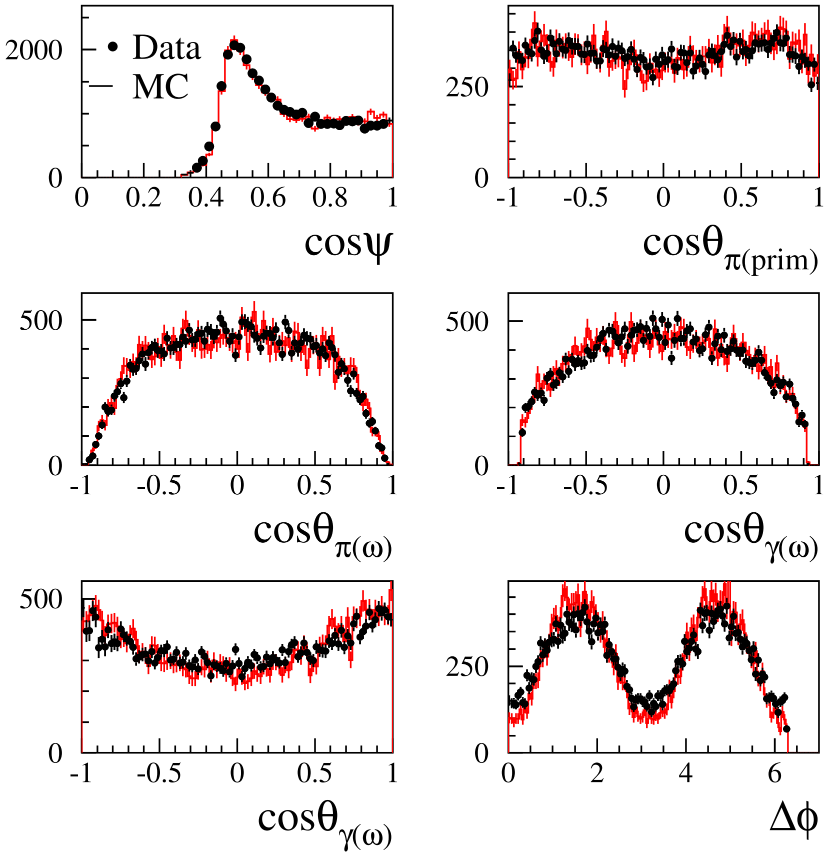

Figure 5: Data-MC comparison of angular distributions for $e^+e^- \to \omega\pi^0 \to \pi^0\pi^0\gamma$ events after background subtraction: $\cos\psi$ and polar angle of the primary π^0 in LRF (top), polar angle for the π^0 and γ produced in the radiative decay of the ω (middle) and $\cos\theta_\gamma$ and $\cos\phi$ evaluated in HRF.

ω decay show a better, even if not perfect, agreement.

3.3 MC expectations for signal and background

The expected rate for the resonant backgrounds is obtained using KLOE results for the cross sections [15, 17] and BRs from [10]. The quantity of $e^+e^- \to \gamma\gamma$ events is instead

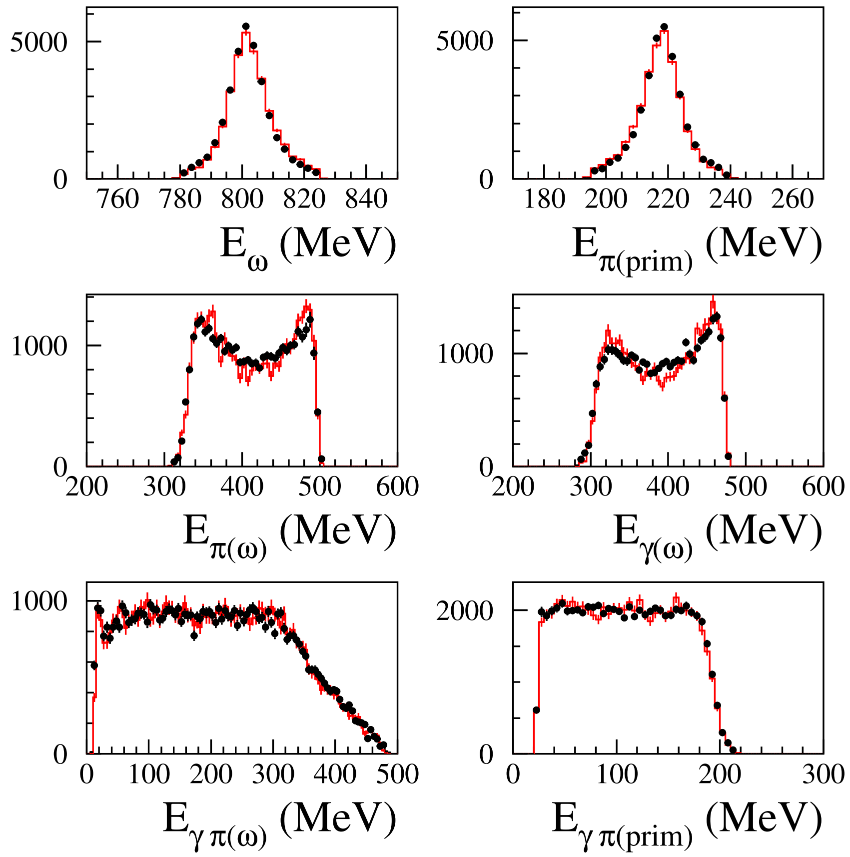

Figure 6: Data-MC comparison of energy distributions for $e^+e^- \to \omega\pi^0 \to \pi^0\pi^0\gamma$ events after background subtraction: energy spectrum for ω and π^0 produced in the collision (top), energy spectrum for the π^0 and γ produced in the radiative decay of the ω (middle) and distribution of photon energy spectrum for the γ's coming from the π^0 from ω and from the primary π^0 (bottom).

obtained directly from data, as described in Par. 6.1. For the two signal processes the same iterative procedure used for 2000 data [6] is applied to evaluate the relative fraction of these decays. The resulting rates for all decays are then used to weight the relative components of MC events in order to have an absolute comparison with data.

4 Sample selection, kinematic fitting and photon pairing

The starting point of the analysis is the acceptance selection of events with the expected final state signature, that is five photons coming from the interaction region (IR). We then retain events with 5 neutral clusters in the expected time window (TW), defined as $|T_\gamma - R_\gamma/c| < \mathrm{MIN}(5\,\sigma_T, 2\text{ ns})$. T_γ and R_γ are the reconstructed time and position of the cluster, while σ_T is the time resolution parametrized as in [11]. The cutoff at 2 ns is inserted to reduce the contribution of accidental coincidence with low energy machine background clusters. Energy and angular acceptance cuts are applied on clusters in the photon counting in order to minimize the machine background and to exclude the region around QCAL: $E_\gamma > 7$ MeV and $|\cos\theta_\gamma| < 0.92$.

One of the most difficult category of background to be evaluated is the $e^+e^- \to \gamma\gamma$, since the cross section is much larger than the signal and the three addition prompt photons are generated either by radiation, by technical clustering problems such as splitting or by accidental coincidence with machine background clusters. In Fig. 7 we show for the two most energetic clusters in the event the distribution of $\phi_1 - \phi_2$ as a function of $E_1 + E_2$. In the data the high energy region is dominated by $\gamma\gamma$ events. Rejecting all events with $E_1 + E_2 > 900$ MeV, we have a large reduction of this kind of events without loosing efficiency for the signal. The calibration of the residual background will be shown in Par. 6.1.

One of the most technical points we have to face in this analysis is the method of pairing photons to π^0. In Ref. [6], we assumed that the processes $\omega\pi$ and $S\gamma$ did not interfere and therefore we developed two different pairing procedures. In more detail, the pseudo-χ^2 we built for the first process had a contribution related to the ω mass and width. In this analysis instead, we are attacking the problem in a more unbiased way. We want to treat in the same way the two processes, leaving to the fit to the Dalitz plot the estimate of the different contributions and their eventual interference. For these reason we have used MC events to find the most efficient method of pairing photons while maintaining at the same time the dependence as a function of $M_{\pi\pi}$ and $M_{\pi\gamma}$ as flat as possible. The new method is based on the following steps:

1. application of a kinematic fit the five photon sample;

2. parametrization of the photon energy resolution after step 1. by Montecarlo;

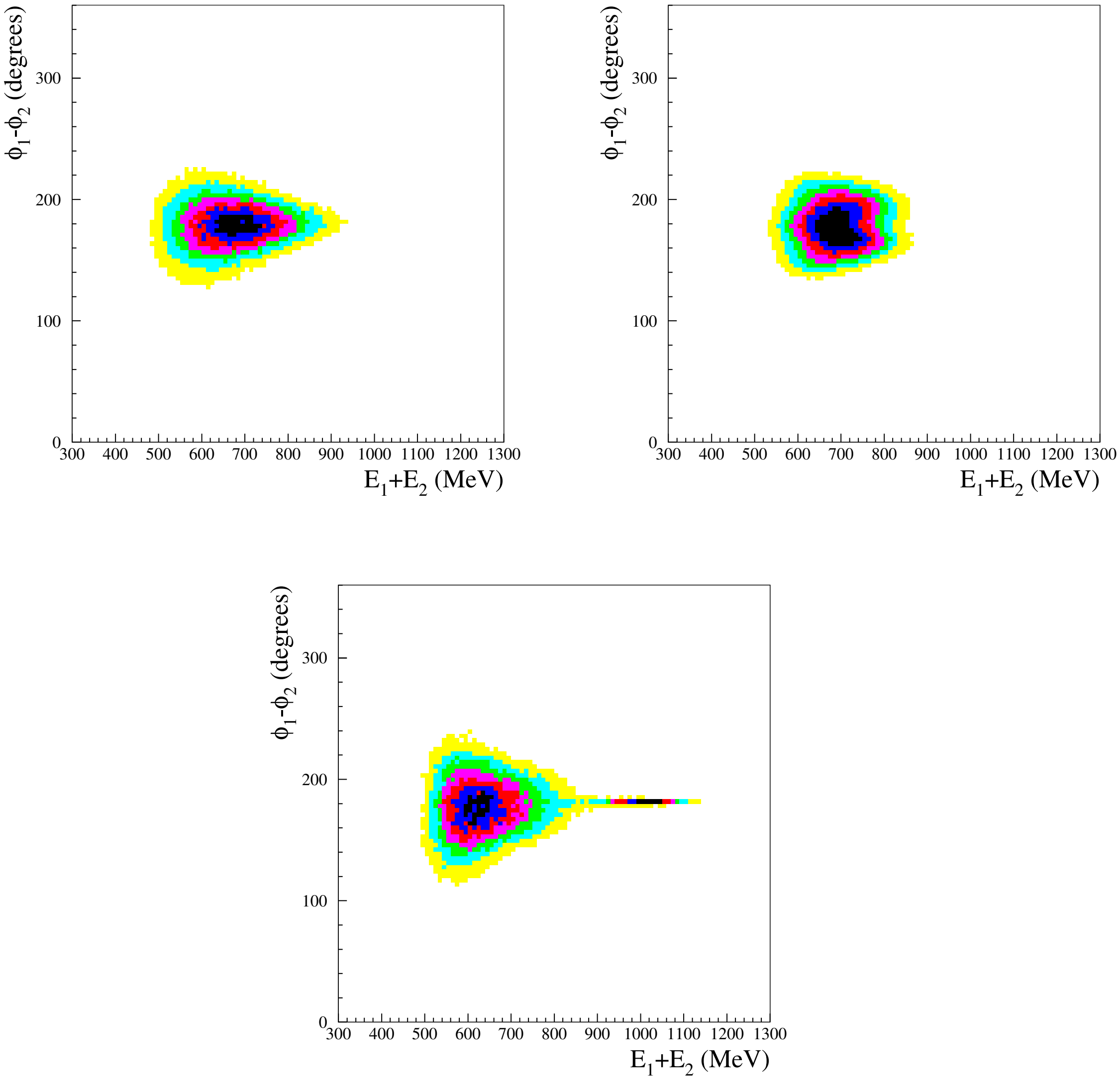

Figure 7: Difference of the azimuthal angle as a function of the sum of energy for the two most energetic photons in the event. As can be seen in the upper distributions (MC: left $S\gamma$, right $\omega\pi$), the signal is concentrated in the region $E_1 + E_2 < 900$ MeV. In the data (bottom) the band visible in the high energy region is due to $e^+e^- \to \gamma\gamma(\gamma)$ events.

3. building of a χ^2 variable for the π^0 reconstruction.

4.1 Kinematic fit

A kinematic fit based on the least squared method [19] is applied to the the five photon sample in order to ensure a kinematic closure of the event. This significantly improves the energy resolution. The 30 free parameters of the fit are: energy, time of flight and position of each cluster (3×5), the energy of the two beams (2) and the three coordinates of the IR (3). The fit constraints, and thus the number of degrees of freedom (ndf), are 9: energy-momentum conservation (4) and the requirement $T_\gamma - R_\gamma/c = 0$ for each photon (5).

4.2 Pairing algorithm

Using the output of the kinematic fit, we studied by Montecarlo the photon energy resolution for $S\gamma$ and $\omega\pi$ processes. The dependence of this resolution as a function of the photon energy after fitting, E_{Fit1}, is reported in Fig. 8. A good reproduction of the data is obtained with the following function, with three free parameters:

$$\frac{\sigma_E}{E} = \frac{P_1 + P_2 \cdot E[\mathrm{MeV}]}{E[\mathrm{GeV}]^{\,1/P_3}}\,, \tag{1}$$

The parameter values are reported in Fig. 8.

The π^0 mass resolution is then parametrized as a function of the quadratic sum of the photon energy resolution:

$$\frac{\sigma_{M_{\pi^0}}}{M_{\pi^0}} = \frac{1}{2}\left(\frac{\sigma_{E_1}}{E_1} \oplus \frac{\sigma_{E_2}}{E_2}\right) \tag{2}$$

The photon combination where four out of the five photons of the event minimize the pseudo-χ^2

$$\mathrm{h}^2 = \frac{(M_{\gamma_i\gamma_j} - M_\pi)^2}{\sigma^2_{M_{ij}}} + \frac{(M_{\gamma_k\gamma_l} - M_\pi)^2}{\sigma^2_{M_{kl}}}\,, \tag{3}$$

χ^2_{sel}, is selected as the good one.

In the evaluation of h^2, the parameters obtained by MC are used also for data. A test of the good MC behaviour can be done by looking at the shapes of the χ^2 variables after the sample selection, reported in Fig. 9 for the most populated bin of $\sqrt{s}$. Only very loose

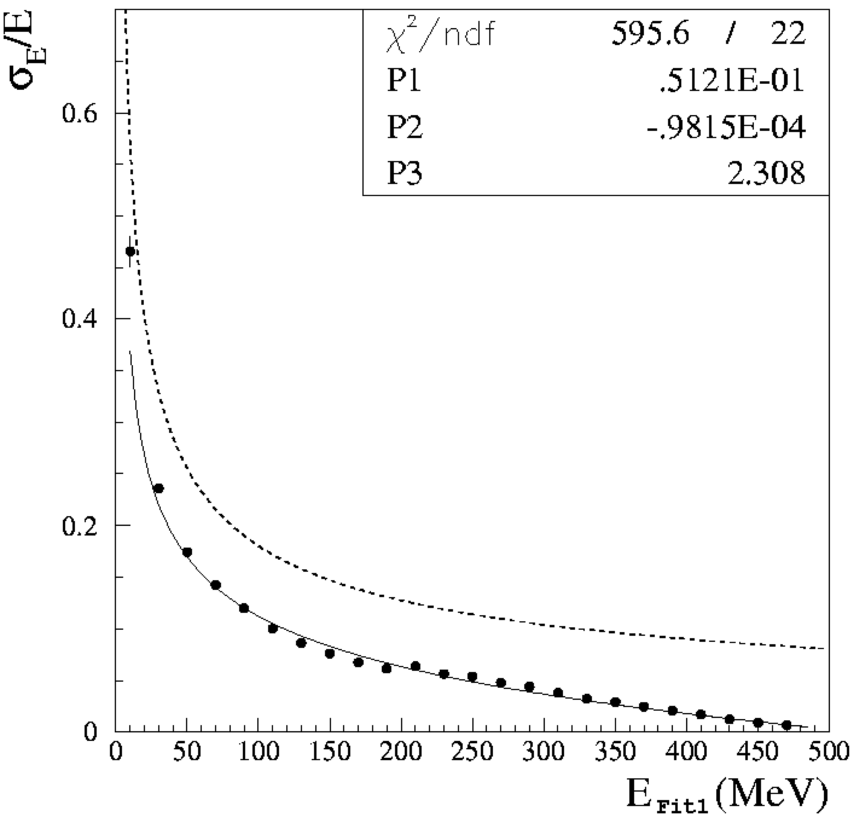

Figure 8: Energy resolution for photons after the first kinematic fit. The dotted line represents the calorimeter energy resolution.

cuts on the total energy and missing momentum were applied to the five photon sample: $E_{\text{tot}} > 800$ MeV and $p_{\text{miss}} < 200$ MeV.

To understand how well this algorithm works, we have counted by MC the fraction of events where all π^0's are correctly matched, using the information of the original particle stored in the cluster. We call this ratio pairing efficiency ($\varepsilon_{\text{pair}}$). In Fig. 10 the dependences of $\varepsilon_{\text{pair}}$ as a function of $M_{\pi\pi}$ and $M_{\pi\gamma}$ are reported. The overall efficiency is $\sim$ 85%, but both $S\gamma$ and $\omega\pi$ processes show a drop in a specific region of the $M_{\pi\pi}$–$M_{\pi\gamma}$ plane ($M_{\pi\pi} \sim 650$ MeV and $M_{\pi\gamma} \sim 200$ MeV for $\omega\pi$, $M_{\pi\pi} \sim 1000$ MeV and $M_{\pi\gamma} \sim 200$ MeV for $S\gamma$). This happens because, on those particular configurations, the energy distribution of

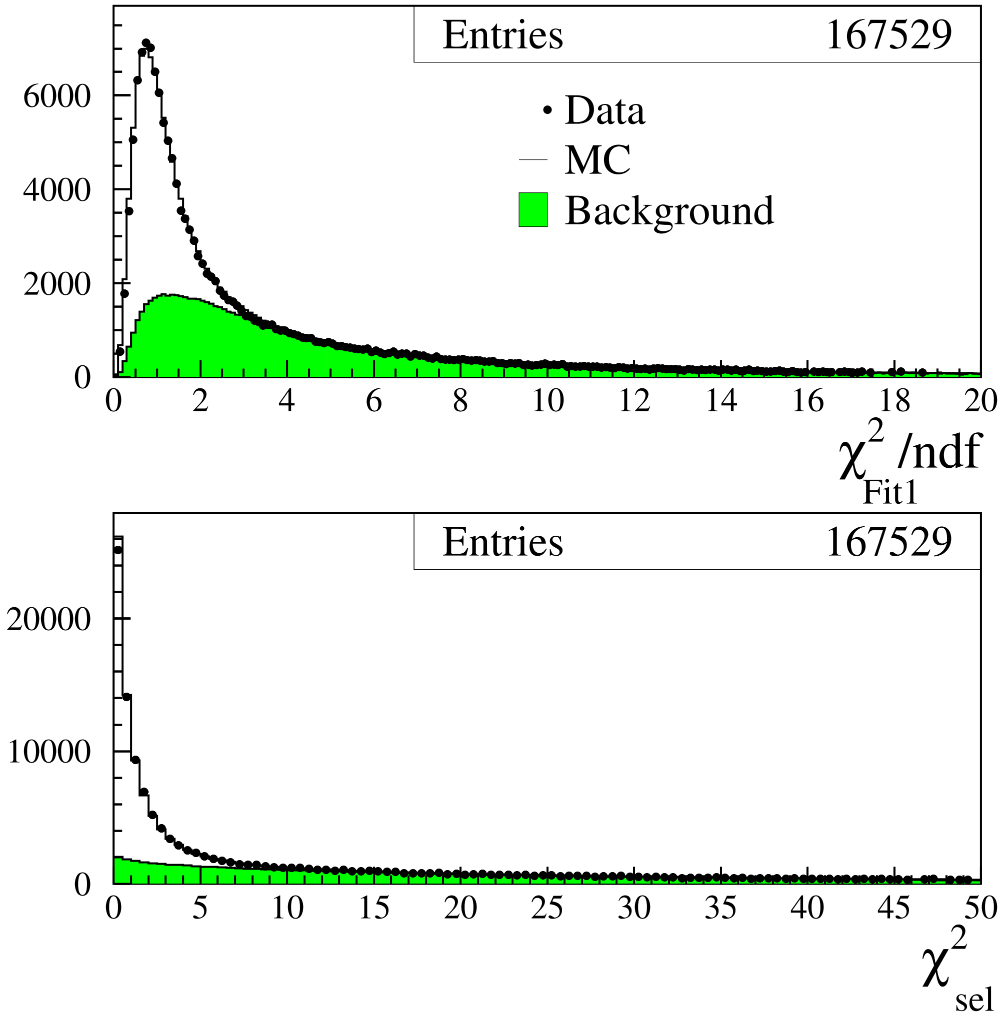

Figure 9: Data-MC comparison after sample selection: normalized χ^2 from the kinematic fit (top) and the minimum value of the pseudo-χ^2 used to pair photons (bottom). Only runs with $\sqrt{s} = 1019.75$ MeV are shown.

the two pions in the event are very similar, causing a higher probability of wrong photon pairing.

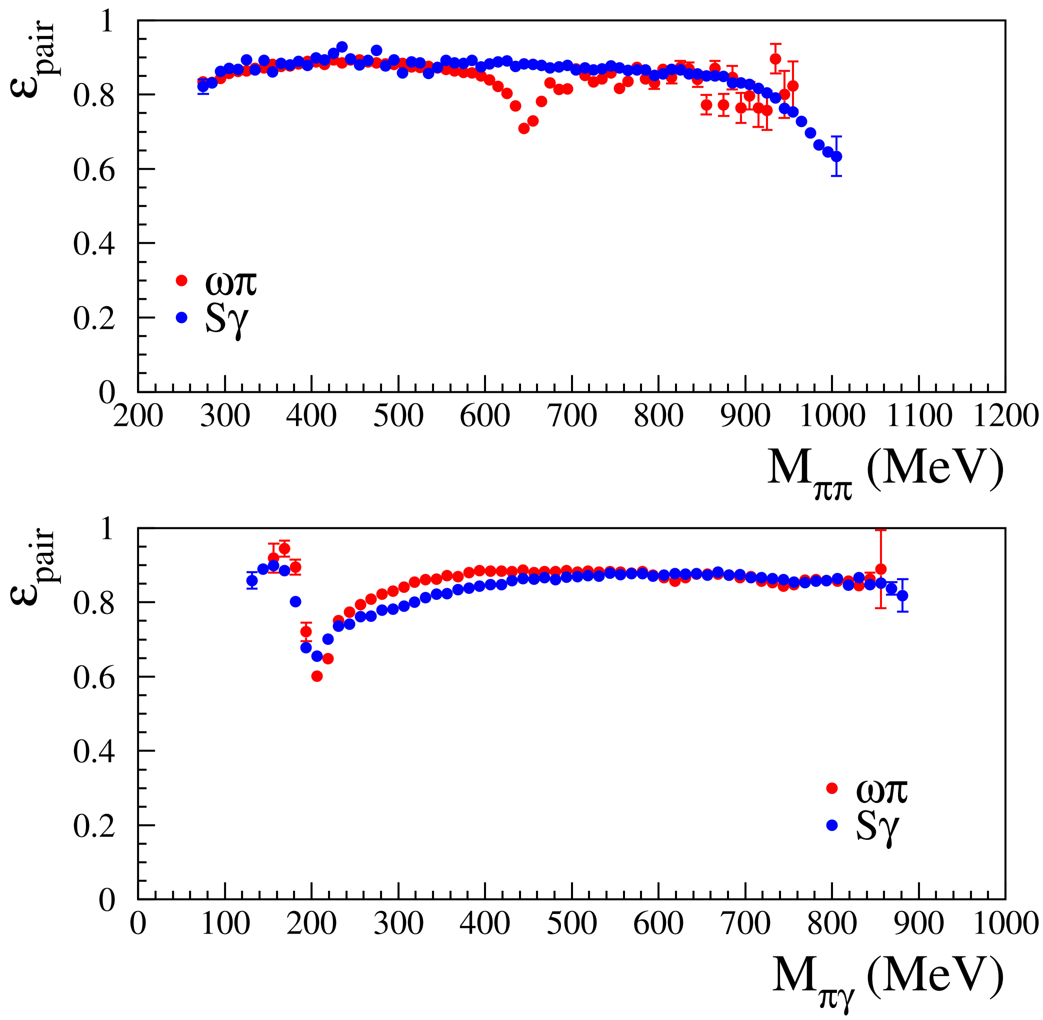

Figure 10: Efficiency of good photon pairing into π^0's for both $S\gamma$ and $\omega\pi$ Montecarlo events.

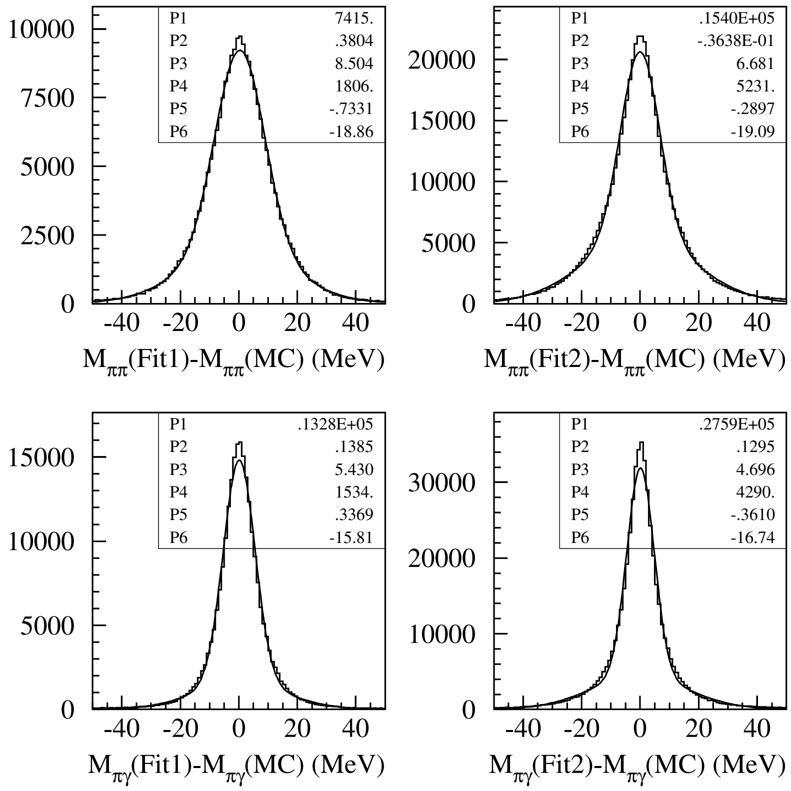

Figure 11: MC mass resolution for $S\gamma$ events after first (left) and second (right) kinematic fit. The upper distributions are for the $\pi^0\pi^0$ invariant mass while the lower ones for the two possible combinations of the $\pi^0\gamma$ invariant mass.

5 Analysis cuts

After the acceptance selection, $\gamma\gamma$ rejection and after having paired the photons to π^0's, the analysis proceeds with the construction of a second kinematic fit which imposes also the mass of the two pions. The total number of constraints is now 11. This second fit improves the mass resolution from a typical value of ≈ 9 MeV (Fit1) to ≈ 5 MeV (Fit2), as shown in Figs. 11, 12. The normalized distribution of $\chi^2_{\rm Fit2}$ is shown for both signal and background in Fig. 13 for the $\sqrt{s}$-bin with higher statistics. The agreement is very

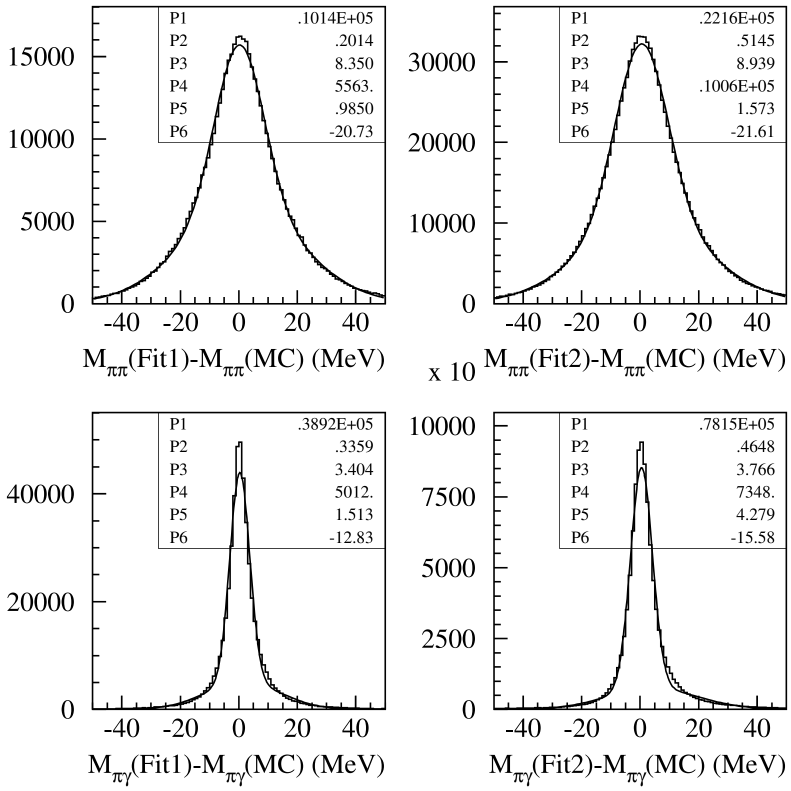

Figure 12: MC mass resolution for $\omega\pi$ events after first (left) and second (right) kinematic fit. The upper distributions are for the $\pi^0\pi^0$ invariant mass while the lower ones for the two possible combinations of the $\pi^0\gamma$ invariant mass.

good both in the tail (top) and in the low χ^2 region of the distribution (bottom).

It is evident that the background can be significantly reduced by cutting on $\chi^2_{\rm Fit2}$. In Tabs. 4, 5 we summarize the changes in the analysis efficiency and in the S/B ratio when hardening this cut. The best overall background rejection, with a still high analysis efficiency for the signal, is obtained for $\chi^2_{\rm Fit2}/{\rm ndf} < 3$. However, by applying this cut on the scalar term the efficiency dependence on the Dalitz plot variables remains flat and there is only a constant drop (Fig. 14), while for the $\omega\pi$ term the efficiency shows a

Process	ε_{ana} (acc)	ε_{ana} ($\chi^2_{\text{Fit2}}/\text{ndf} < 3$)	ε_{ana} ($\chi^2_{\text{Fit2}}/\text{ndf} < 5$)
$S\gamma$	$(52.7 \pm 0.1)\%$	$(48.7 \pm 0.1)\%$	$(50.3 \pm 0.1)\%$
$\omega\pi$	$(55.85 \pm 0.05)\%$	$(50.23 \pm 0.04)\%$	$(53.12 \pm 0.05)\%$
$\eta\pi\gamma$	$(52.5 \pm 0.1)\%$	$(18.7 \pm 0.1)\%$	$(23.2 \pm 0.1)\%$
$\eta\gamma_7$	$(77.08 \pm 0.05) \cdot 10^{-3}$	$(3.62 \pm 0.01) \cdot 10^{-3}$	$(8.51 \pm 0.02) \cdot 10^{-3}$
$\eta\gamma_3$	$(14.85 \pm 0.07) \cdot 10^{-4}$	$(5.83 \pm 0.04) \cdot 10^{-4}$	$(8.15 \pm 0.05) \cdot 10^{-4}$
$\pi\gamma$	$(9.2 \pm 0.2) \cdot 10^{-4}$	$(2.28 \pm 0.05) \cdot 10^{-4}$	$(3.07 \pm 0.06) \cdot 10^{-4}$
$\gamma\gamma$	$(2.25 \pm 0.04) \cdot 10^{-5}$	$(0.09 \pm 0.01) \cdot 10^{-5}$	$(0.19 \pm 0.01) \cdot 10^{-5}$

Table 4: Analysis efficiency for different cuts on χ^2_{Fit2}, compared with the value obtained at the level of the acceptance selection. Errors include only the statistical uncertainty on Montecarlo.

Process	S/B (acc)	S/B ($\chi^2_{\text{Fit2}}/\text{ndf} < 3$)	S/B ($\chi^2_{\text{Fit2}}/\text{ndf} < 5$)
$\eta\pi\gamma$	8.8	22.6	18.9
$\eta\gamma_7$	0.5	8.7	3.9
$\eta\gamma_3$	18.8	43.4	32.3
$\pi\gamma$	121.8	448.0	346.1
$\gamma\gamma$	37.2	804.2	407.5

Table 5: Signal over background ratio for different cuts on χ^2_{Fit2}, compared with the value obtained at the level of the acceptance selection.

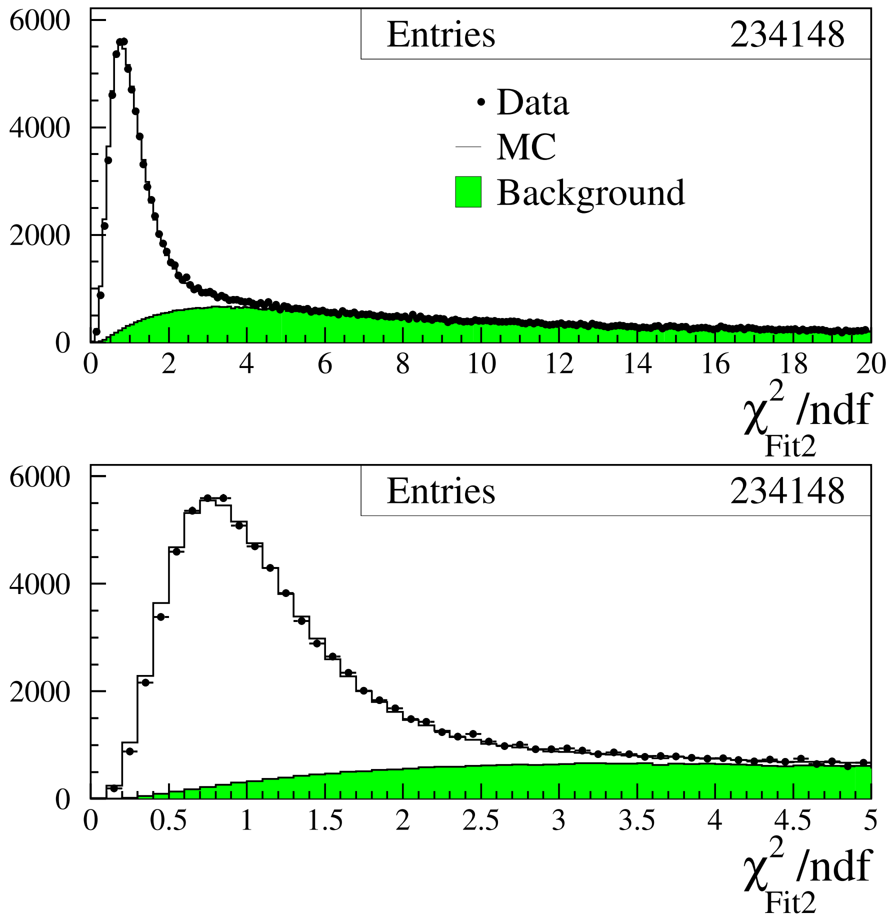

Figure 13: Data-MC comparison after sample selection: normalized χ^2 from the second kinematic fit. Only runs with $\sqrt{s} = 1019.75$ MeV are shown.

structure along $M_{\pi\pi}$ and $M_{\pi\gamma}$ and the drop is not constant (Fig. 15). This is related to the not-resonant behaviour of the $\omega\pi$ cross-section and to the spectrum of the radiated photons in conjunction with our constraint of $E_{\mathrm{tot}} = \sqrt{s}$. More detail on this problem can be found in App. B. The chosen compromise is to retain all events with $\chi^2_{\mathrm{Fit2}}/\mathrm{ndf} < 5$, using at the same time a more precise description of the radiative tails.

The good data quality can be appreciate in Figs. 16, 17, where the data-MC agreement

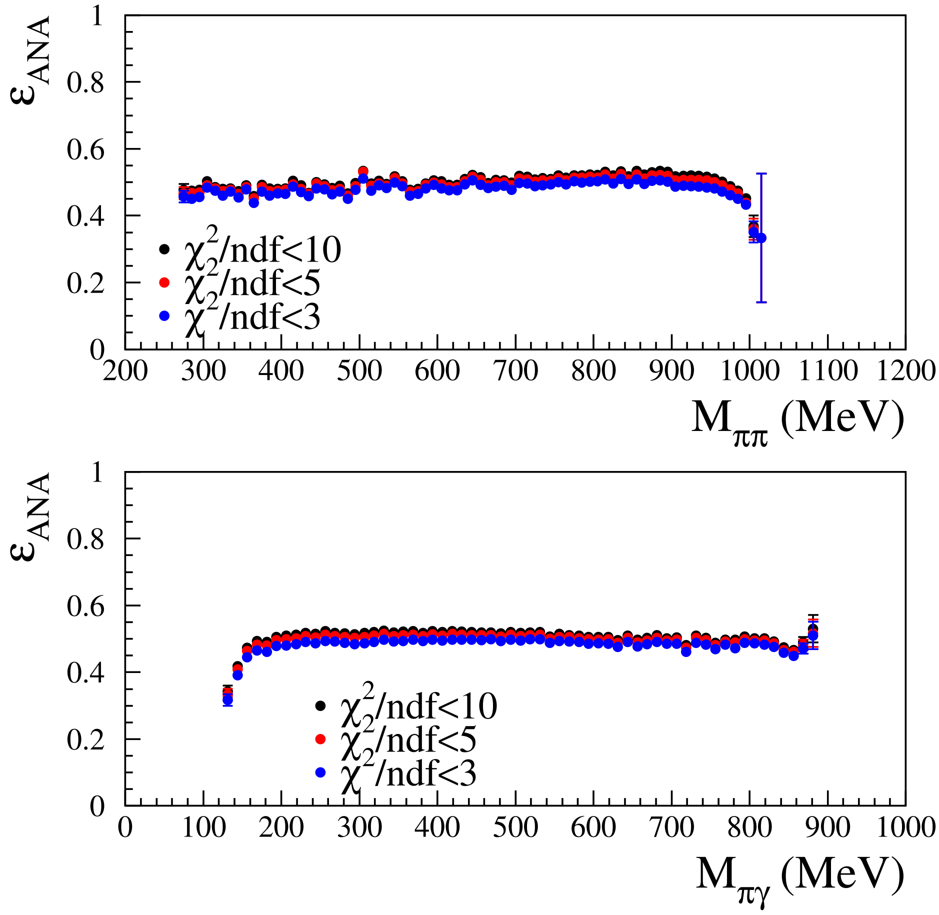

Figure 14: Analysis efficiency for $S\gamma$ MC events as a function of $M_{\pi\pi}$ and $M_{\pi\gamma}$. Except for the boundaries of the Dalitz plot the efficiency is flat, showing a small constant drop when the cut on χ^2_{Fit2} is hardened.

after the χ^2_{Fit2} cut is shown for the distributions of the photon energy and for the $\Delta M_\pi/\sigma$ variable of the two reconstructed π^0's. This last variable represents the difference of the $\gamma\gamma$ invariant mass from the nominal π^0 mass normalized by the expected mass resolution parametrized as in (2). In order to remove the background surviving in the tails of the last quantity, a loose cut is applied and only events with $|\Delta M_\pi/\sigma| < 5$ are retained for

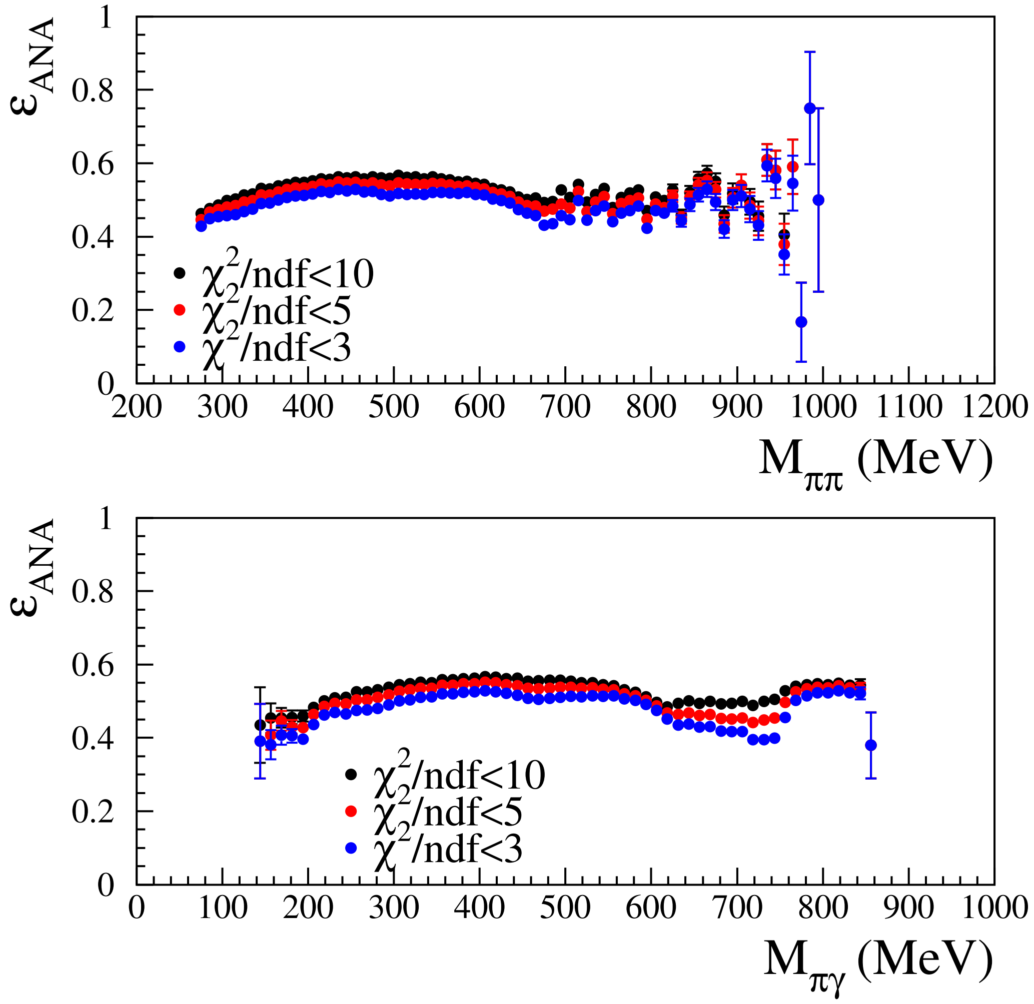

Figure 15: Analysis efficiency for $\omega\pi$ MC events as a function of $M_{\pi\pi}$ and $M_{\pi\gamma}$. The efficiency is not flat along the Dalitz plot variables, showing an increasing drop in the region $M_{\pi\gamma} \approx 700$ MeV when hardening the cut on $\chi^2_{\rm Fit2}$.

further analysis.

The data-MC comparison of the two Dalitz plot variables after all the analysis cuts is shown in Fig. 18. While the agreement on $M_{\pi\gamma}$ is good, showing that the precision on the VMD description in our Montecarlo is enough, there are some discrepancies in $M_{\pi\pi}$, especially in the region where the scalar contribution dominates. This can be due either

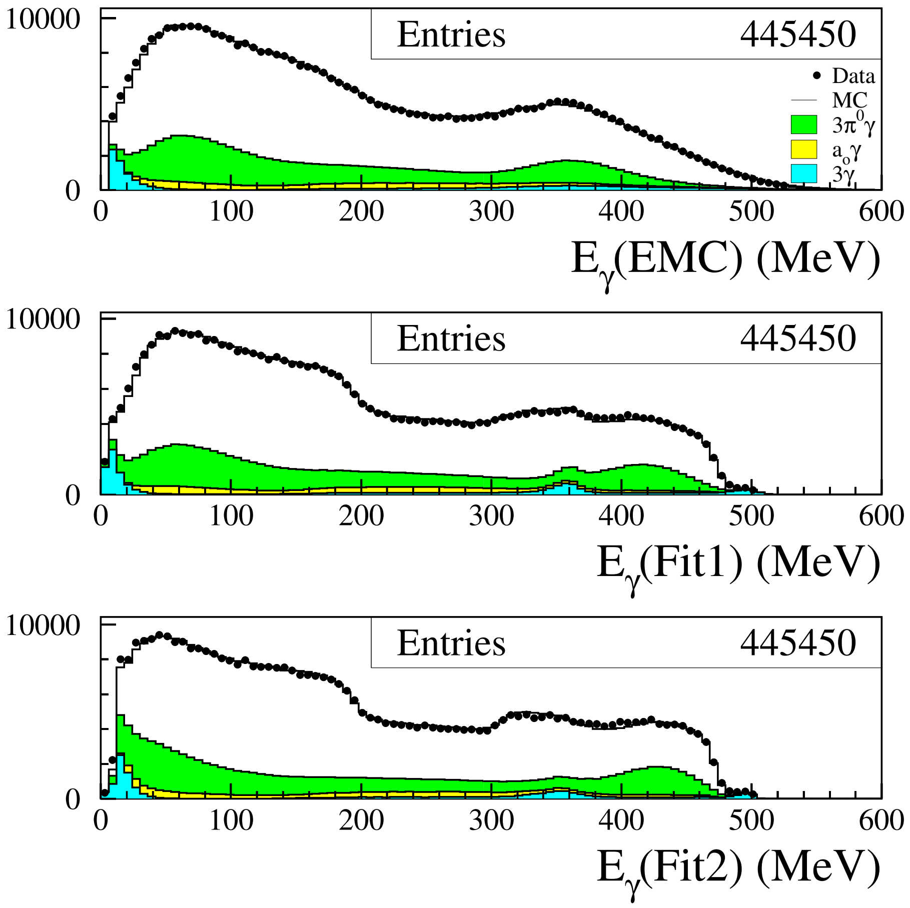

Figure 16: Data-MC comparison after $\chi^2_{\rm Fit2}$ cut: photon energy distribution using calorimeter information (top) and the output of Fit1 (middle) and Fit2 (bottom). Only runs with $\sqrt{s} = 1019.75$ MeV are shown.

to a not good description of the scalar mass spectrum or to a possible interference between the two $\pi^0\pi^0\gamma$ final states. This last possibility is exploited in Ref. [8], where a complete fit to the Dalitz plot is performed.

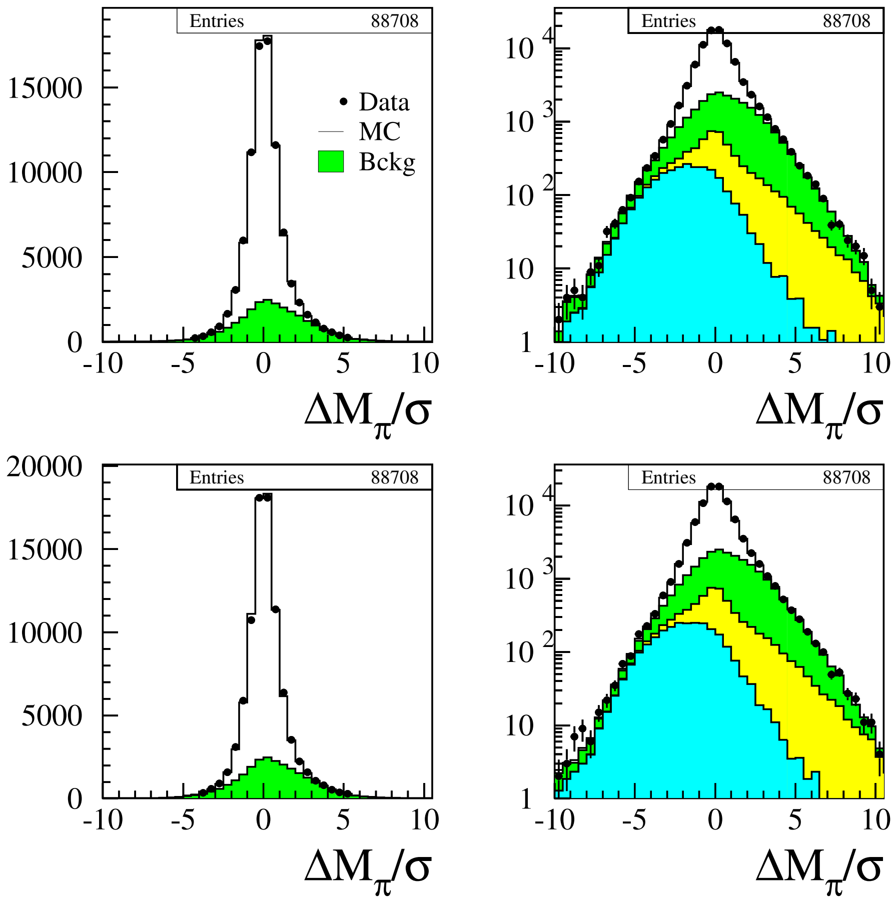

Figure 17: Data-MC comparison after $\chi^2_{\rm Fit2}$ cut: normalized π^0 mass of the two selected pair of photons, evaluated using Fit1 output variables. For the distributions in logarithmic scale, the colour labels are the same of Fig. 16. Only runs with $\sqrt{s} = 1019.75$ MeV are shown.

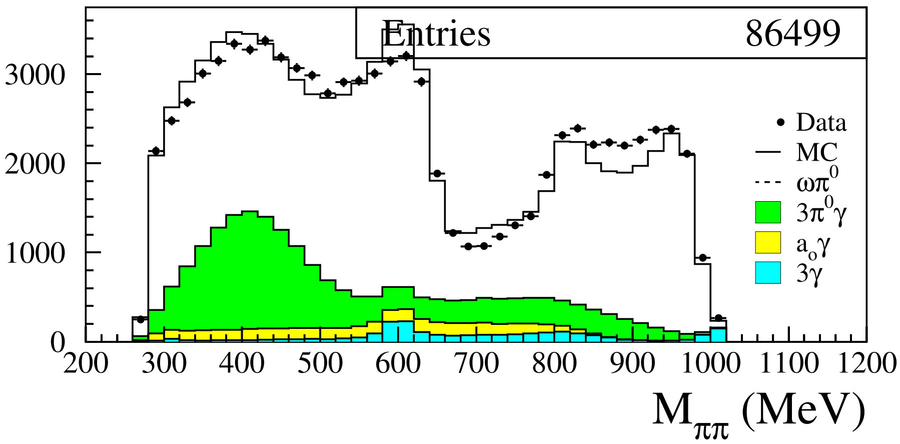

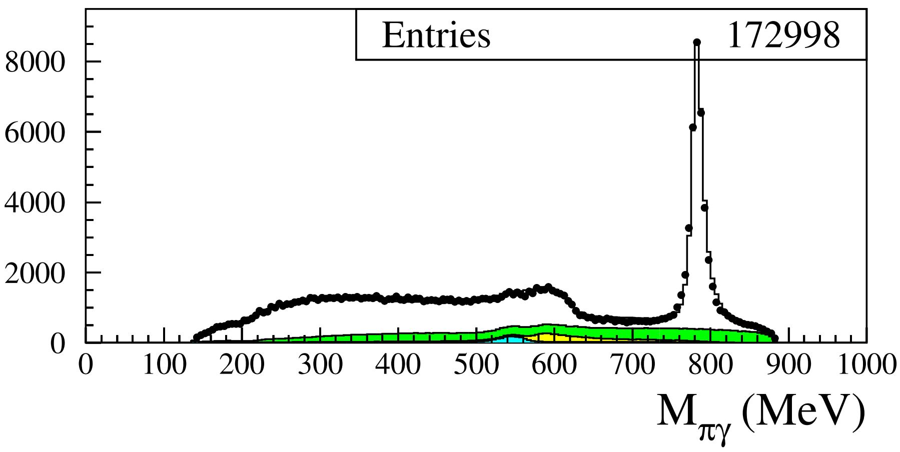

Figure 18: Data-MC comparison after all cuts: invariant mass for the two Dalitz plot variables, $M_{\pi\pi}$ (top) and $M_{\pi\gamma}$ (bottom). Only runs with $\sqrt{s} = 1019.75$ MeV are shown.

Process	δBR/BR	δB/B
$\gamma\gamma$	—	1.6%
$\eta\gamma_7$	3.0%	3.2%
$\eta\gamma_3$	3.5%	7.0%
$\pi^0\gamma$	10.0%	68.0%
$\eta\pi^0\gamma$	9.5%	7.5%

Table 6: Relative systematic uncertainties on the background estimate. The first column represents the errors on the applied BRs while the second one is the error coming from the fit to the background-enriched distributions.

6 Systematics on background evaluation

As already shown in Tab. 1, we have many background sources with very different cross section and topology. Therefore we cannot simply trust the Montecarlo to estimate their rate and their shape before subtracting their contribution from data. Hence, as discussed in Par. 3.3, we have first cross-checked, for each source, the MC rates with the latest estimates on literature [10], using also KLOE measurements when available. We have then found some background-enriched distributions to further calibrate our expectations and check the Montecarlo shapes. The calibration is done by fitting the data ($\mathrm{H_{data}}$) with two MC components: the background we are considering ($\mathrm{H_{bckg}}$) and all the other contributions, including also the $\pi^0\pi^0\gamma$ signal ($\mathrm{H_{others}}$):

$$\mathrm{H_{data}} = \alpha_1\,\mathrm{H_{bckg}} + \alpha_2\,\mathrm{H_{others}} \tag{4}$$

Apart from $\gamma\gamma$ events, we do not apply these scale factors but instead we assign a maximal systematic error of $\delta B = (1-\alpha_1)/2$. The corresponding relative errors δB/B for all background channels are listed in Tab. 6, together with the uncertainties on the BRs.

6.1 $e^+e^- \to \gamma\gamma(\gamma)$

As previously stated, this source of background is dangerous in some mass region, expecially for $M_{\pi\pi}$ close to M_ϕ. To test how well we control this process we remove the $\gamma\gamma$ rejection, applying only the χ^2_{Fit2} cut, and we fit the $\phi_1 - \phi_2$ distribution with (4).

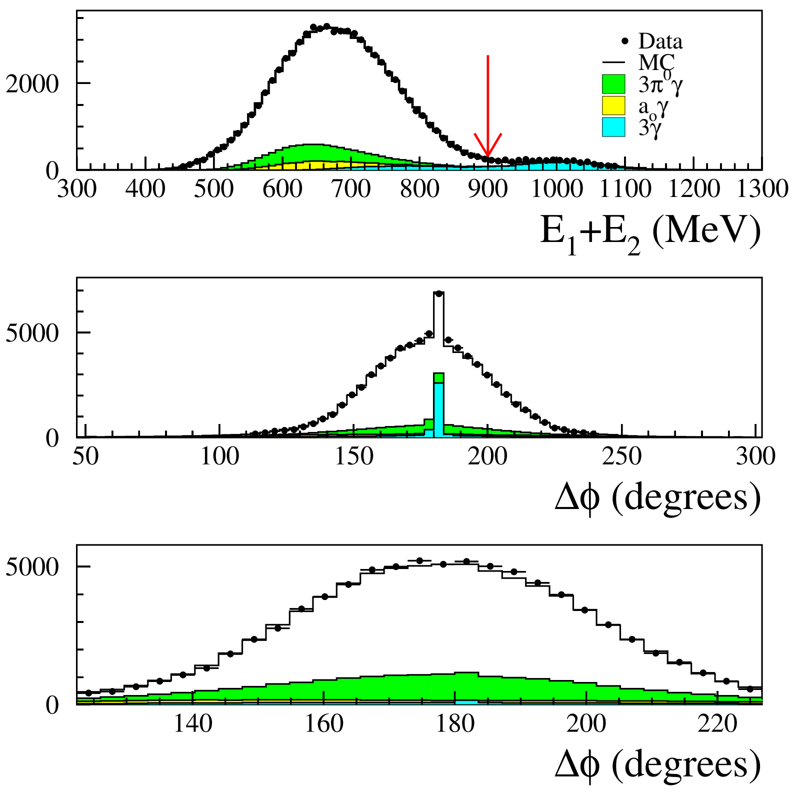

Figure 19: Data-MC comparison for events with $\chi^2_{\mathrm{Fit2}}/\mathrm{ndf} < 5$, removing the $\gamma\gamma$ rejection: sum of energy (top) and difference of the azimuthal angle (middle) for the two most energetic photons of the event. The $\phi_1 - \phi_2$ distribution after all the analysis cuts is shown in the bottom plot. Only runs with $\sqrt{s} = 1019.75$ MeV are shown.

The Montecarlo significantly fails to reproduce its rate, probably due to a higher probability in data of having multiple radiative photons or additional clusters in the event. The calibration factor $\alpha_1 = 1.85 \pm 0.03$ is then used to correct the amount of this background. The $E_1 + E_2$ and $\phi_1 - \phi_2$ distributions after rescaling $\gamma\gamma$ events are reported in Figs. 19.top/middle, showing a good data-MC agreement in the regions where this background dominates. Anyhow, the residual contamination after the $E_1 + E_2$ cut is very small, as shown in Fig. 19.bottom.

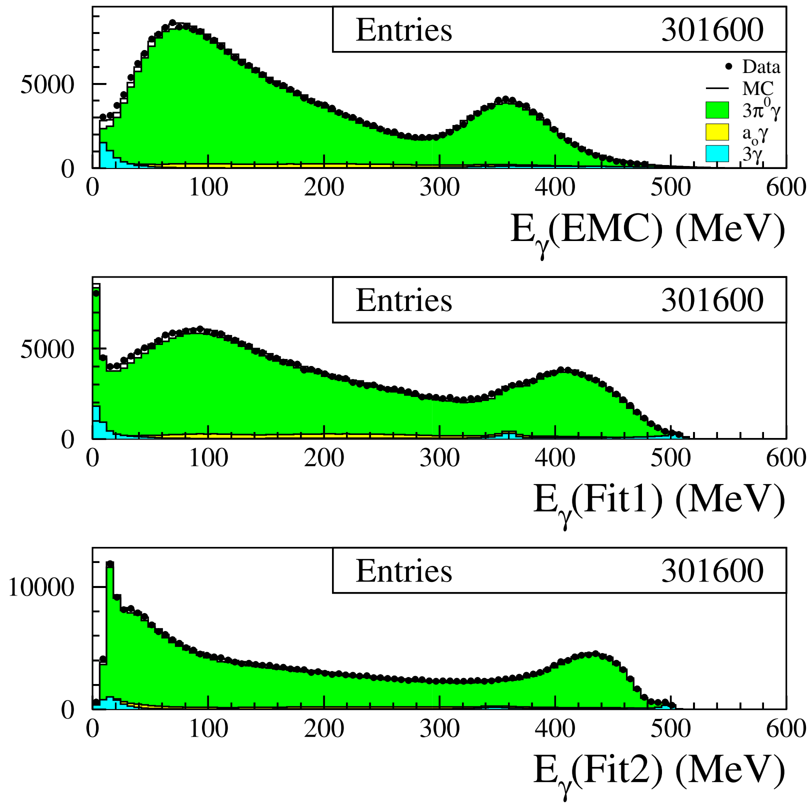

Figure 20: Data-MC comparison for events with $4 < \chi^2_{\rm Fit2}/{\rm ndf} < 20$: photon energy distribution using calorimeter information (top) and the output of Fit1 (middle) and Fit2 (bottom). Only runs with $\sqrt{s} = 1019.75$ MeV are shown.

6.2 $\phi \to \eta\gamma \to \pi^0\pi^0\pi^0\gamma$

This is the largest background and it is dominating the region at high $\chi^2_{\rm Fit2}$ values. We have then studied its rate and shape in the interval $4 < \chi^2_{\rm Fit2}/{\rm ndf} < 20$. In Fig. 20, the distributions of E_γ for all photons before and after kinematic fitting are shown. The green area is the one expected by this category of events. The Montecarlo well reproduces the background. Fitting the E_γ(EMC) distribution, we get a scale factor $\alpha_1 = (1.064 \pm 0.002)$, which provides a systematic error of the same order of the BR uncertainty.

In Figs. 21, 22 other data-MC comparison for this background enriched sample are

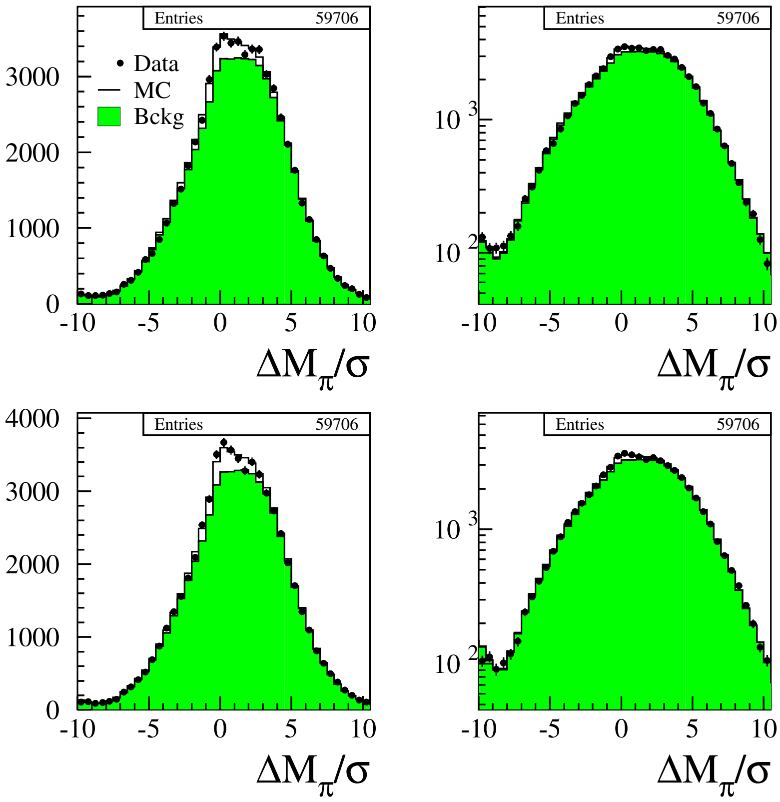

Figure 21: Data-MC comparison for events with $4 < \chi^2_{\mathrm{Fit2}}/\mathrm{ndf} < 20$: normalized π^0 mass of the two selected pair of photons, evaluated using Fit1 output variables. The small white solid histogram represents the amount of $\pi^0\pi^0\gamma$ signal events expected by MC. Only runs with $\sqrt{s} = 1019.75$ MeV are shown.

shown. A good data-MC agreement both for the π^0 invariant mass and the χ^2 distributions is observed.

6.3 $\phi \to \eta\gamma \to \gamma\gamma\gamma$ and $\phi \to \pi^0\gamma$

As for the $\gamma\gamma$ events, these two backgrounds are small in size at the end of the analysis, entering in our data sample because of the presence of two additional clusters, either by splitting or machine background. In both cases, using three out of five photons, we

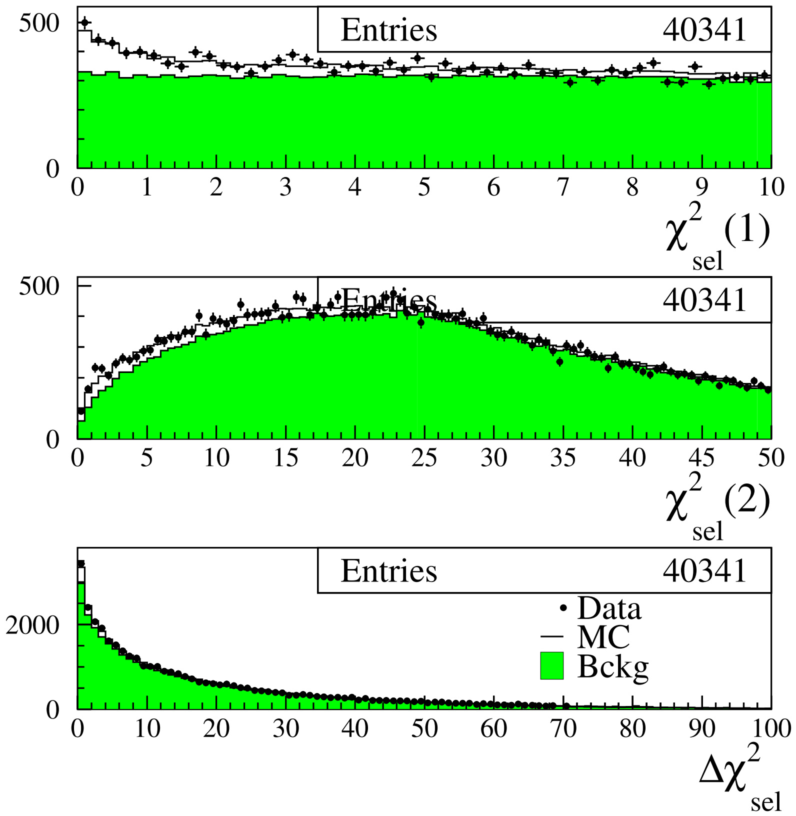

Figure 22: Data-MC comparison for events with $4 < \chi^2_{\rm Fit2}/{\rm ndf} < 20$: distribution of the best (top) and second-best (middle) combinations for the pseudo-χ^2 used to pair photons. The difference between the two is shown in the bottom plot. Only runs with $\sqrt{s} = 1019.75$ MeV are shown.

minimize a χ^2 variable including the pesudoscalar mass (M_P, where P is η or π^0) and the energy of the primary photon (E_p):

$$\chi^2 = \frac{(M_{\gamma_1\gamma_2} - M_P)^2}{\sigma_M^2} + \frac{(E_{\gamma_3} - E_p)^2}{\sigma_E^2}\,. \tag{5}$$

The combination that minimizes the χ^2, $\chi^2_{\eta\gamma 3}$ or $\chi^2_{\pi\gamma}$ for the two hypotheses, is chosen as the good one.

In the $\chi^2_{\eta\gamma 3}$ distribution, the peak due to $\eta\gamma_3$ process is clearly visible (Fig. 23.top),

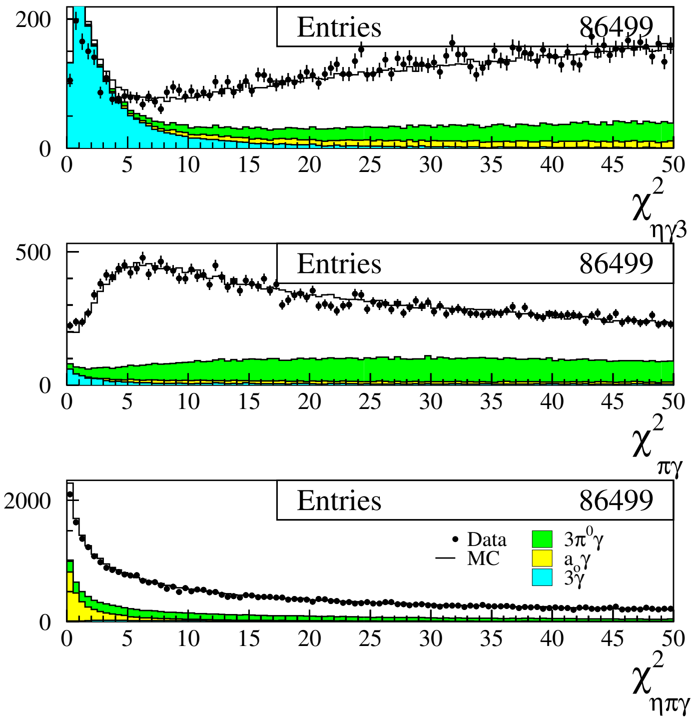

Figure 23: Data-MC comparison after all analysis cuts: minimum value for the pseudo-χ^2 used to pair photons in the $\eta\gamma_3$ (top), $\pi\gamma$ (middle) and $\eta\pi\gamma$ (bottom) hypotheses. Only runs with $\sqrt{s} = 1019.75$ MeV are shown.

suggesting an excess of MC events. Indeed, we find $\alpha_1 = (0.86 \pm 0.02)$. On the other end, for the $\pi^0\gamma$ background, where the S/B ratio is very high, the peak in the $\chi^2_{\pi\gamma}$ distribution is overwealmed by all the other processes (Fig. 23.middle). The fit gives $\alpha_1 = (2.35 \pm 0.02)$.

6.4 $\phi \to \eta\pi^0\gamma$

Also in this case we built a χ^2 variable, using the two masses of the intermediate state:

$$\chi^2 = \frac{(M_{\gamma_1\gamma_2} - M_\eta)^2}{\sigma^2_{M_\eta}} + \frac{(M_{\gamma_3\gamma_4} - M_{\pi^0})^2}{\sigma^2_{M_\pi}}\,. \tag{6}$$

Again, the combination that minimizes the χ^2, $\chi^2_{\eta\pi\gamma}$, is chosen as the good one. The $\chi^2_{\eta\pi\gamma}$ is reported in Fig. 23.bottom and the fit result is $\alpha_1 = (0.86 \pm 0.02)$.

7 Systematics on event counting

The evaluation of the systematics connected to the event counting is reported in this section. We have subdivided the possible origin of systematics in four main sources: the preselection, which includes the trigger, the filter of background and the event classification, the definition of the cluster counting, the analysis cuts and the procedure of photon pairing.

7.1 Preselection

The preselection of the events starts with the request of a calorimeter based trigger. As shown in Ref. [6], we are fully efficient on the signal. The only losses we can have are related to the cosmic ray veto (CV) which requires at least two cosmic sectors above 30 MeV. We evaluated the CV losses with 2001 data, using prescaled events.[3] Since in 2002 there was the T3 filter running, recovering some of the cosmic veto losses, we keep the same correction of 2001, disregarding the events with a CV flag in data. The total efficiency correction to be applied to the data is found to be

$$\varepsilon_{\rm CV} = (\,99.54 \pm 0.08\,)\,\%\,. \tag{7}$$

We have then estimated the efficiency of the filter for the rejection of the machine background, Filfo, which is based on calorimeter information only [21]. Using simulated data we measured its efficiency to be $\varepsilon^{\rm MC}_{\rm FLF} = (99.95 \pm 0.01)\%$. Although this is a very small loss, we have cross checked with data this determination. A special prescaled minimum bias sample was created for the 2001-2002 data sample by applying on raw data a very loose event selection for the radiative decays [22]. We consistently find

$$\varepsilon_{\rm FLF} = (\,99.90 \pm 0.05\,)\,\%\,. \tag{8}$$

In a similar manner we have also estimated the losses due to the event classification filter (ECL). In the Montecarlo signal we find a rather low classification efficiency, $\varepsilon^{\rm MC_{SIG}}_{\rm ECL} = (96.5 \pm 0.1)\%$. When using the minimum bias sample we instead obtain

$$\varepsilon_{\rm ECL} = (\,99.2 \pm 0.1\,)\,\%\,. \tag{9}$$

[3] In the streamed data the events vetoed by the cosmic veto are retained with a prescaling factor of 50.

The origin of such a discrepancy has been found to be due to a wrong parametrization of the time resolution in the code running on the simulated data. We have then applied a correction factor to the event classification MC efficiency, $\varepsilon_{\rm ECL}/\varepsilon_{\rm ECL}^{\rm MC_{SIG}}$. The systematic error assigned to this correction was evaluated by applying to a sub-sample of Montecarlo events the ECL algorithm with the corrected parametrization of the time resolution. Considering also the fraction of background events surviving the analysis cuts, we found an efficiency $\varepsilon_{\rm ECL}^{\rm MC_{ALL}} = 98.5\%$. The systematic error assigned to the event classification is then half of the difference between this value and the efficiency obtained from data: $\delta\varepsilon_{\rm ECL}/\varepsilon_{\rm ECL} = 0.5\,(\varepsilon_{\rm ECL} - \varepsilon_{\rm ECL}^{\rm MC_{ALL}})/\varepsilon_{\rm ECL} = 0.35\%$.

The overall effect of the preselection is at the end a correction factor on the MC analysis efficiency of $R_{\rm presel} = \varepsilon_{\rm ECL}/\varepsilon_{\rm ECL}^{\rm MC_{SIG}} \times \varepsilon_{\rm FLF} \times \varepsilon_{\rm CV} = 1.022 \pm 0.004$.

7.2 Cluster counting

The counting of five photons in a prompt time window, with an energy cutoff and in a given angular region, constitutes our acceptance after preselection. The main sources of the discrepancy between data and Montecarlo are related to the MC energy scale and the simulation of the clustering efficiency. Following Ref. [24], we evaluated by Montecarlo the changes in efficiency when applying an energy scale correction of 1.4% to each cluster in the event. For each bin of the Dalitz plot we evaluated the variation in the efficiency and estimated the relative systematic error as $(\varepsilon_{\rm NEW} - \varepsilon_{\rm OLD})/\varepsilon_{\rm OLD}$. In Fig. 24.left-top this value is compared with the error due to the statistics and background subtraction for each bin of the Dalitz plot.

Using a sample of $\phi \to \pi^+\pi^-\pi^0$ events, the ratio of the data-MC curve as a function of the photon energy has been inserted in the simulation [23]. In Fig. 24.left-middle we show the systematic error due to the variation of this curve, obtained by changing the opening cone used to define the photon acceptance region. In a more recent analysis it has been shown that the MC cluster efficiency correction curve from $\phi \to \pi^+\pi^-\pi^0$ suffers from a residual contamination of Bhabha events [25]. We have studied in a smaller MC sample how much this affects our signal determination. The effect on the analysis efficiency is at the level of few % in the whole $M_{\pi\pi}$ region (Fig. 24.right) and the corresponding systematic effect is comparable to the other effects we have considered (Fig. 24.left-bottom).

The change in the MC cluster efficiency also affects the quantity of residual background

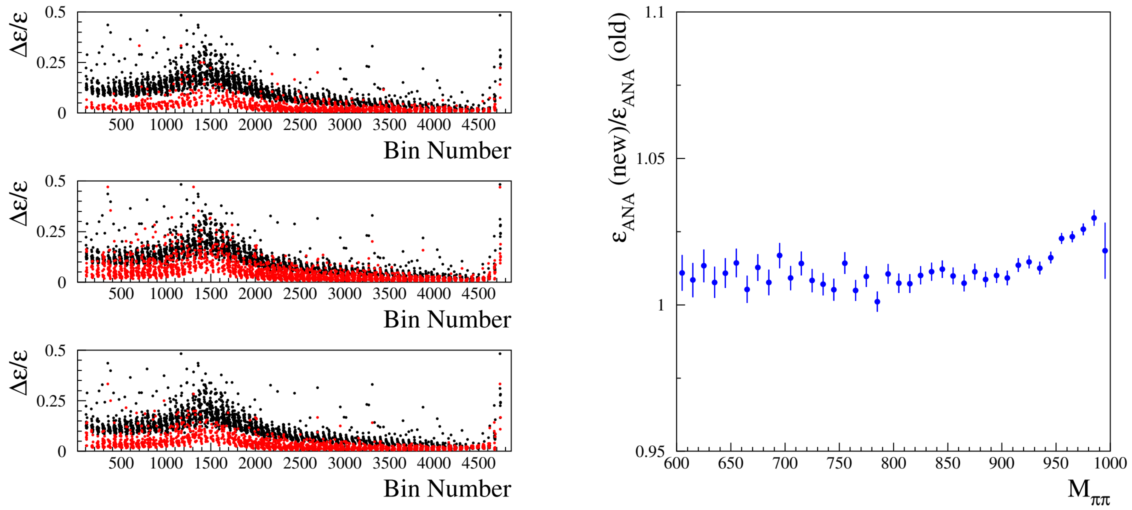

Figure 24: Left: in red, systematic error due to MC energy scale (top), cluster efficiency cone size (middle) and cluster efficiency curve (bottom) as a function of the bin number of the Dalitz plot. Systematics are compared with the statistical+background errors, in black. The bin number is obtained by slicing the Dalitz plot in $M_{\pi\pi}$ and running on $M_{\pi\gamma}$. Right: variation of the analysis efficiency for the two cluster energy curves as a function of the $\pi^0\pi^0$ invariant mass.

at the end of the analysis cuts. This is true especially for $\eta\gamma_7$, where the efficiency plays an important role. For this reason we have considered an additional systematic error, defined as the difference of signal events after background subtraction. In Fig. 25 the relative error due to the MC cluster efficiency is compared with the statistical+background errors on the difference between data and background. The systematic contribution is significantly smaller in the whole Dalitz plot.

We have also considered a possible systematic contribution due to the angular acceptance. For this reason we have studied the data-MC difference in the cumulative distribution of the maximum value of the polar angle in the event (Fig. 26). The effect is completely negligible compared to the cluster efficiency.

The systematic error due to the cluster counting is the quadratic sum of all the contributions we have considered. Integrating all the bins of the Dalitz plot the overall value is $\delta\varepsilon_{\rm clu}/\varepsilon = 1.65\%$.

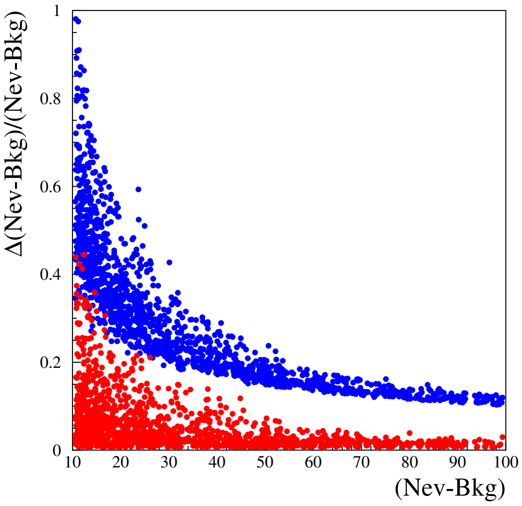

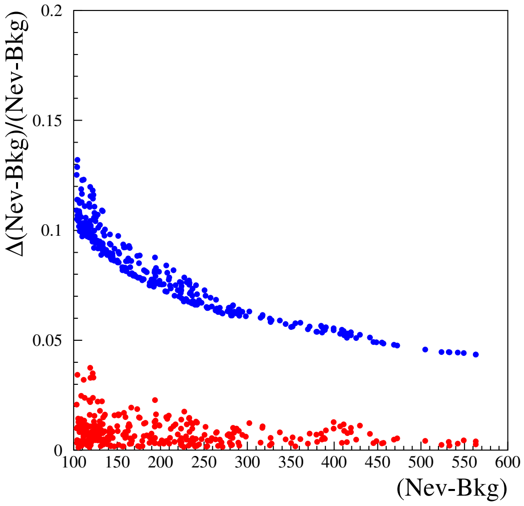

Figure 25: Relative error due to the MC cluster efficiency (red) and the statistical+background errors on the difference between data and background (blue) as a function of the number of events after background subtraction in the Dalitz plot.

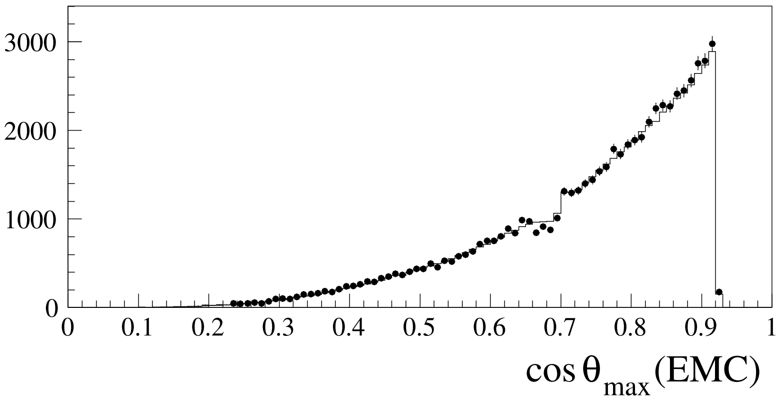

Figure 26: Maximum value of the polar angle of the event for data after background subtraction (black dots) and MC signal (solid histogram). The drop at $\cos\theta_{\text{max}} = 0.7$ is due to a higher failure probability of the clustering algorithm in the barrel-endcap overlap region. Only runs with $\sqrt{s} = 1019.75$ MeV are shown.

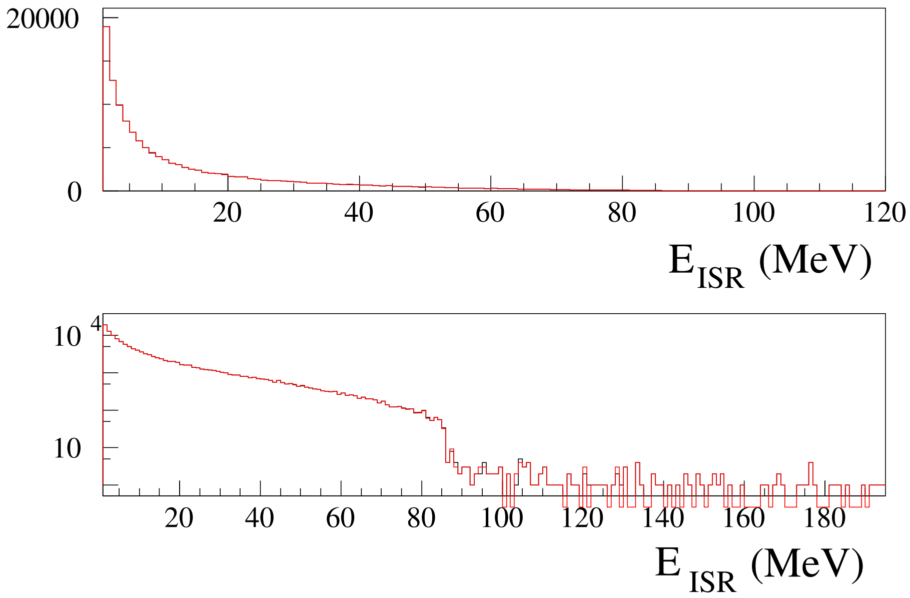

Figure 27: Energy of photons from the Initial State Radiation for $\omega\pi$ events in linear (top) and logarithmic (bottom) scale. The black and red histograms are obtained using the two parametrization of the nude cross section from [26].

7.3 Analysis cuts

After the sample selection, the only two analysis cuts are on the χ^2 of the second kinematic fit (Fig. 13) and on the normalized π^0 masses (Fig. 17). In both cases the systematic error is evaluated from the data-MC difference in the cumulative distribution. The main contribution comes from $\chi^2_{\rm Fit2}$, giving a relative systematic error of 1%.

Another possible source of systematic error on the $\chi^2_{\rm Fit2}$ cut is the MC energy shape of the photon(s) from the Initial State Radiation (ISR) for the $\omega\pi$ process. As discussed in App. B, a difference in the energy spectrum directly reflects in a difference on $\chi^2_{\rm Fit2}$. We have then tried two different parametrizations for the nude cross section used to evaluate the ISR corrections [26]. As can be seen from Fig. 27, the difference of the two ISR energy distributions can be hardly seen. The corresponding systematic error is therefore completely negligible.

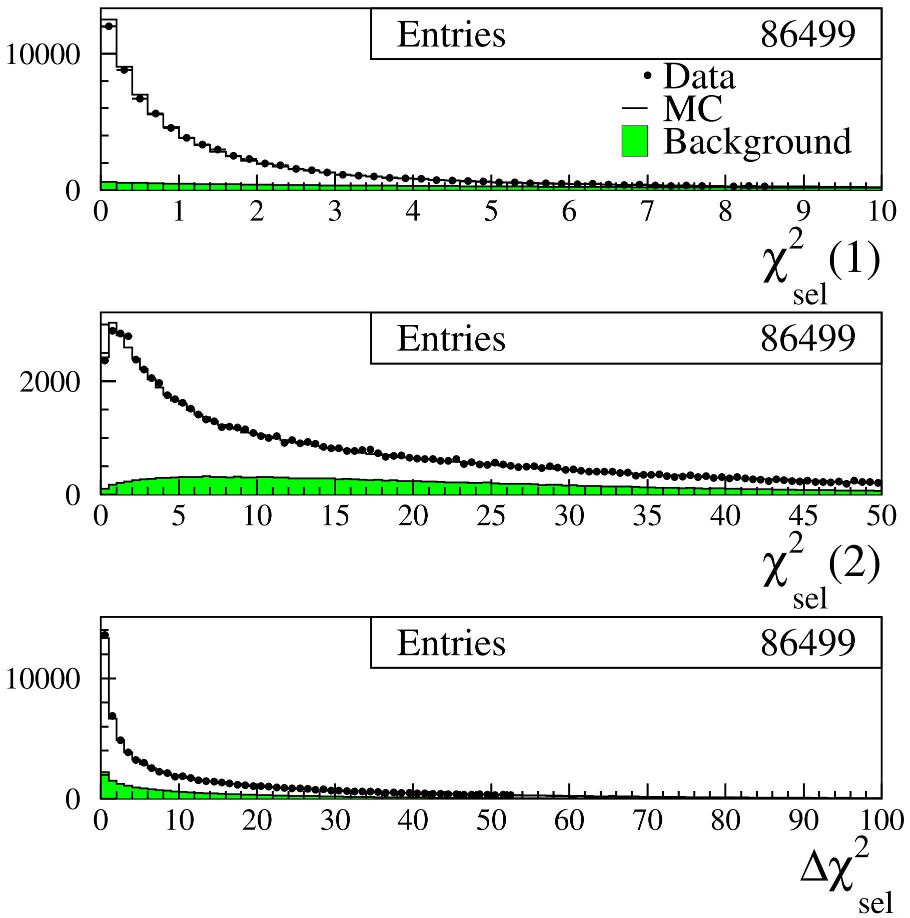

Figure 28: Data-MC comparison for the pseudo-χ^2 used to pair photons: distribution of the best (top) and second-best (middle) combinations and the difference between the two (bottom). Only runs with $\sqrt{s} = 1019.75$ MeV are shown.

7.4 Photon pairing

To measure the percentage of wrong pairing in the data, the difference of the two lowest value for pseudo-χ^2 used to pair photons, $\Delta\chi^2_{\rm sel}$, is used. In Fig. 28 some data-MC comparison for these quantities are shown, while in Fig. 29.top the shape of the $\Delta\chi^2_{\rm sel}$ variable

Source	$\delta\varepsilon/\varepsilon$
Trigger	$8 \cdot 10^{-4}$
Filfo	$5 \cdot 10^{-4}$
Event classification	0.35 %
Clustering	1.65 %
Analysis cuts	1.00 %
Pairing	0.62 %
Total	2.06 %

Table 7: Summary table of the systematic errors due to the event counting.

for good and bad pairing is reported; in the latter case the distribution is concentrated at low values of $\Delta\chi^2_{\rm sel}$. These two templates are used to fit the data (Fig. 29.bottom) by minimizing the variable:

$$X^2 = \sum_i \frac{\left[N^i_{\rm obs} - \alpha(\mathrm{P1}\,N^i_{\rm bad} + \mathrm{P2}\,N^i_{\rm good})\right]^2}{N^i_{\rm obs}} \tag{10}$$

where $N^i_{\rm obs}$, $N^i_{\rm bad}$ and $N^i_{\rm good}$ are the number of events for the three samples (data, correct pairing and wrong pairing respectively) in the i-th bin of $\Delta\chi^2_{\rm sel}$ distributions. The parameter $\alpha = \sum_i N^i_{\rm obs}/\sum_i(\mathrm{P1}\,N^i_{\rm bad} + \mathrm{P2}\,N^i_{\rm good})$ normalizes the MC entries to the number of events in the data. A correction factor $\varepsilon_{\rm pair}(\mathrm{data})/\varepsilon_{\rm pair}(\mathrm{MC}) = (1.08 \pm 0.02)$ is found. The assigned systematic error is therefore half of this correction factor, multiplied by the percentage of events where the photons are wrongly paired to π^0's (15.4% considering the whole Dalitz plot): $\delta\varepsilon_{\rm pair}/\varepsilon = 0.62\%$.

7.5 Summary of systematics on event counting

The summary of the systematic errors on the event counting is reported in Tab. 7. The contributions from the preselection (trigger, Filfo and event classification) are small compared to the systematics related to the analysis (cuts and pairing) and clustering, which dominate the error.

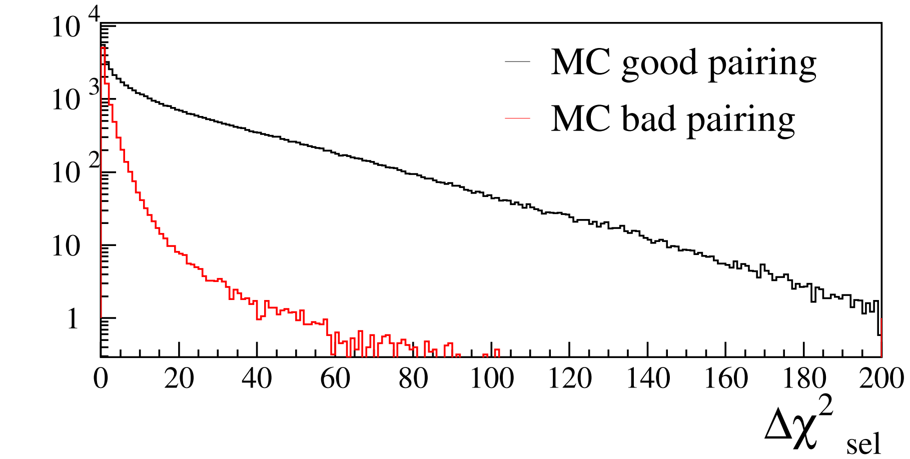

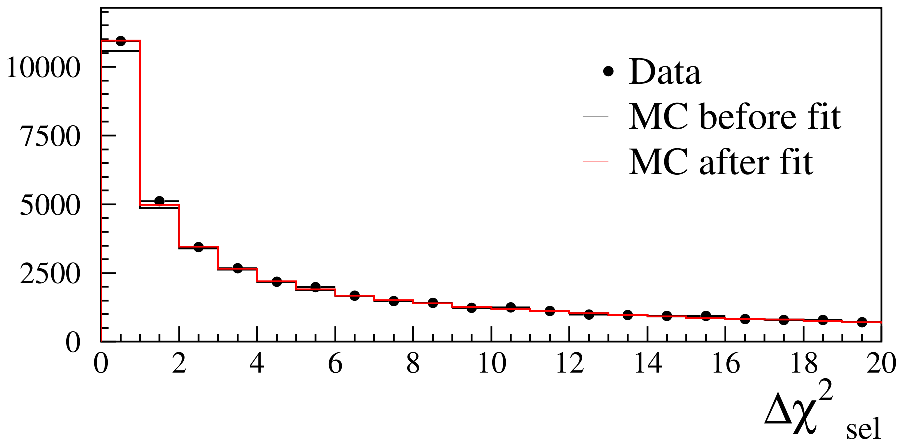

Figure 29: Top: Montecarlo $\Delta\chi^2_{\mathrm{sel}}$ shapes for events with correct and wrong photon pairing. These two templates are used to fit the $\Delta\chi^2_{\mathrm{sel}}$ data distribution (bottom). A better data-MC agreement is obtained after the fit.

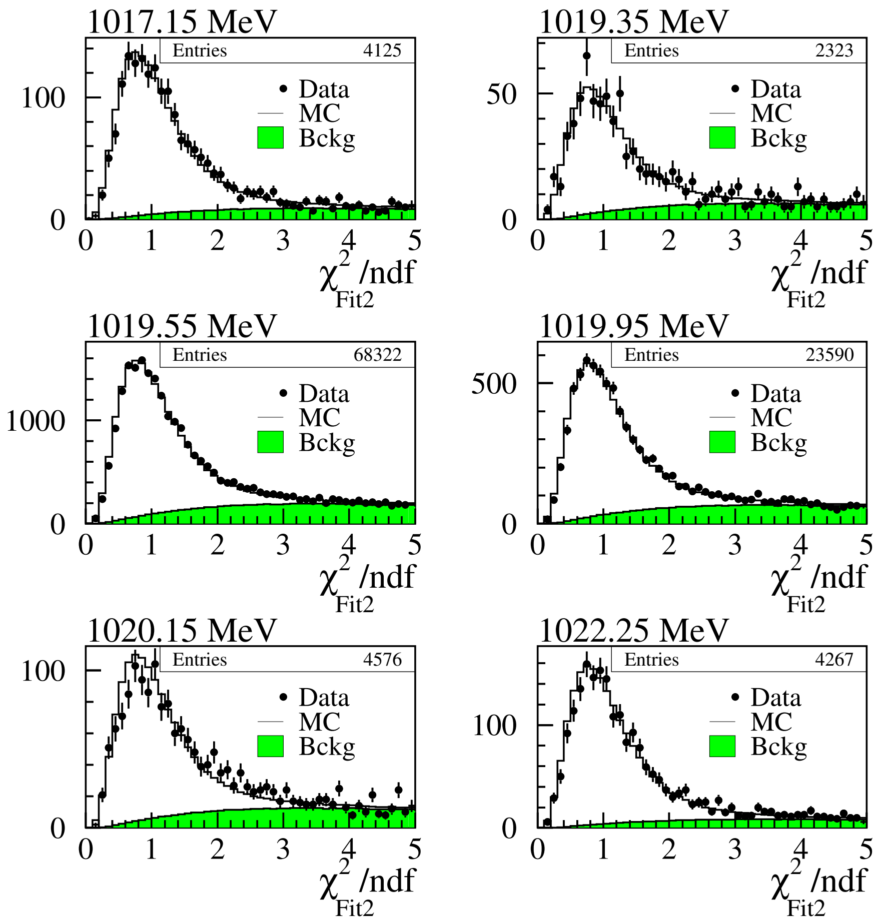

Figure 30: Data-MC comparison for different values of $\sqrt{s}$, specified in the top-left corner of each plot: χ^2_{Fit2} after sample selection.

8 $\sqrt{s}$ dependence of the visible cross sections

The analysis described in the previous paragraphs was tuned using only data from the $\sqrt{s}$ bin with higher statistics. We have then repeated the analysis for all the other center of mass energies. In Figs. 30, 31 and 32 some data-MC comparison for these further data sets are shown. Also here the agreement is very good. In order to have a high Montecarlo statistics in each $\sqrt{s}$ bin, we have used the whole MC production for all the center of mass

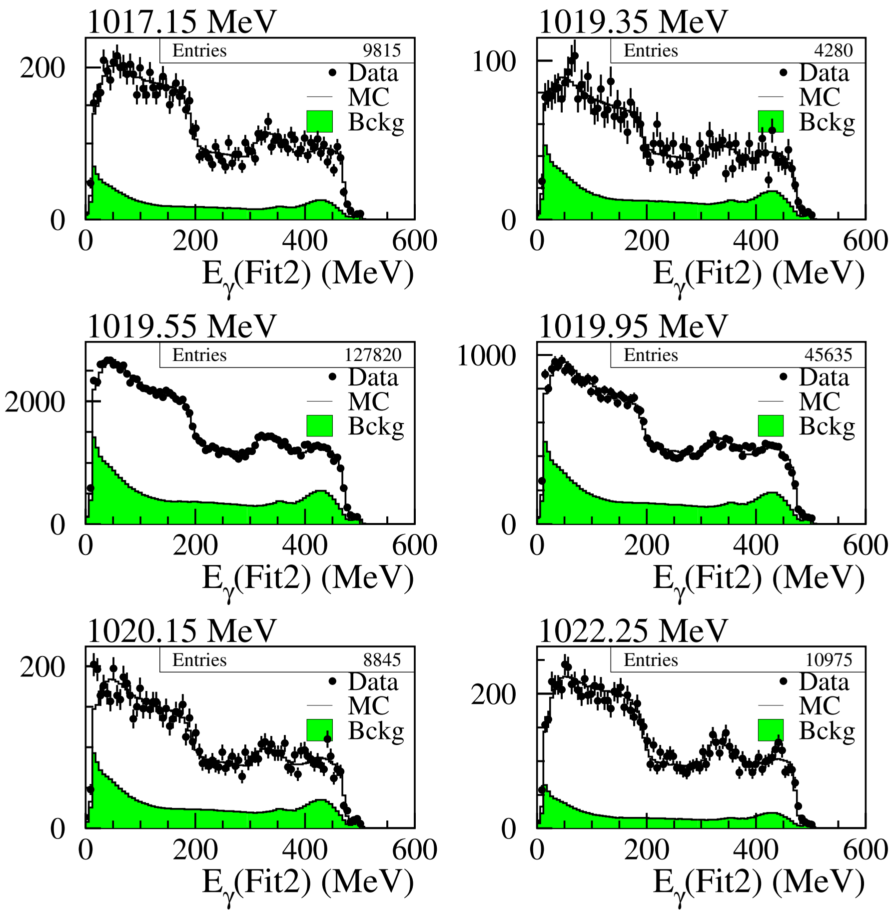

Figure 31: Data-MC comparison for different values of $\sqrt{s}$, specified in the top-left corner of each plot: photon energy from second kinematic fit with χ^2_{Fit2} cut applied.

energies. The analysis efficiency is indeed flat for both the $S\gamma$ and $\omega\pi$ processes in the considered range (see Fig. 33).

The two processes $S\gamma$ and $\omega\pi$, giving the same $\pi^0\pi^0\gamma$ final state, have a very different behaviour as a function of $\sqrt{s}$: the first one is resonant, while the second one is linear, showing a dip at $\sqrt{s} \sim M_\phi$ due to the interference with the $\phi \to \omega\pi^0$ decay [26]. We have than checked these characteristics by studying the behaviour of the cross sections as

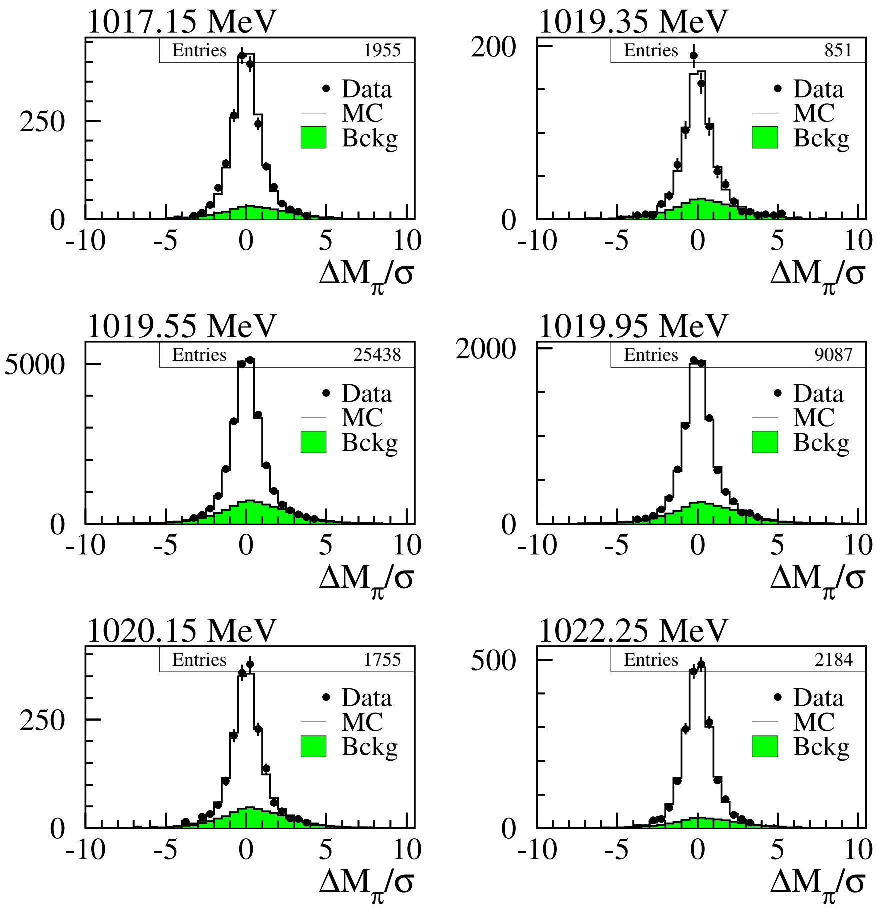

Figure 32: Data-MC comparison for different values of $\sqrt{s}$, specified in the top-left corner of each plot: normalized pion mass from first kinematic fit with χ^2_{Fit2} cut applied.

a function of the center of mass energy.

8.1 Exclusive analysis: $\omega\pi$ *vs* $S\gamma$ events

As already explained before, we want to study the behaviour of the cross section as a function of $\sqrt{s}$ for the processes $S\gamma$ and $\omega\pi$. If we assume that they are uncorrelated, we

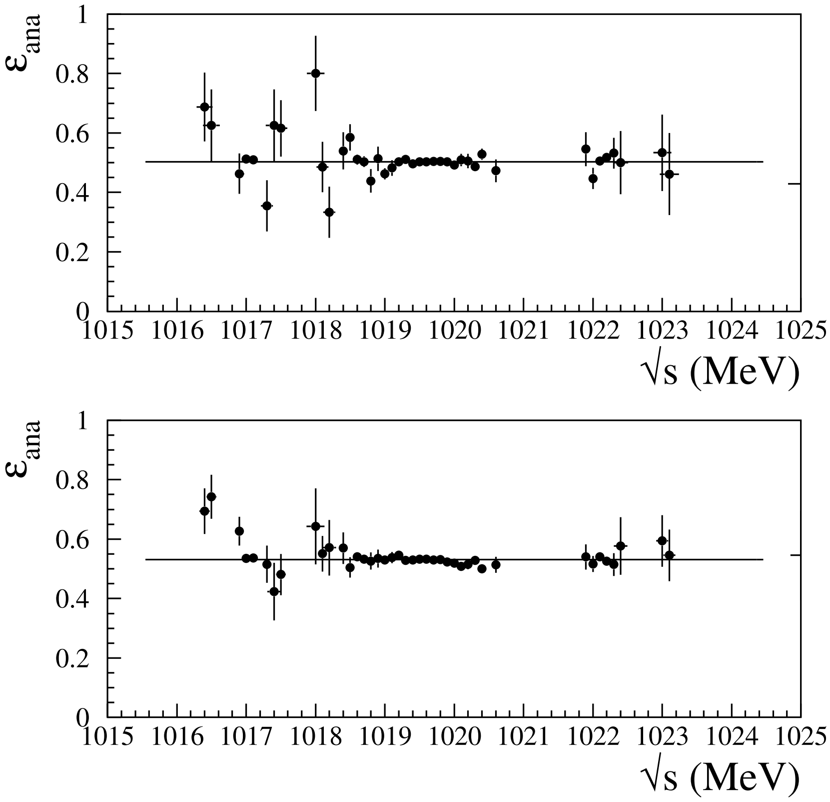

Figure 33: Analysis efficiency as a function of $\sqrt{s}$ for $S\gamma$ (top) and $\omega\pi$ (bottom) Montecarlo events.

can distinguish them by cutting on some appropriate variables. We have then chosen to use the ω mass: the distribution of the $\pi^0\gamma$ invariant mass, whose value is nearer to M_ω, is shown in Fig. 34 after the $\chi^2_{\rm Fit2}$ and ΔM_π cuts. Events with $|M_{\pi\gamma} - M_\omega| < 3\,\sigma_\omega$ are classified as $\omega\pi$ while all the rest is $S\gamma$. Since these two processes cannot be completely separated, at the end of the analysis each of them is a background to the other one. For this reason, as in [6], an iterative procedure is applied to evaluate the relative fraction of these decays, until converging to stable values.

In Fig. 35 the data-MC comparison for the $\cos\theta$ and $\cos\psi$ angular distributions are shown for both $S\gamma$ and $\omega\pi$ processes, using data taken at $\sqrt{s} = 1019.75$ MeV. The two

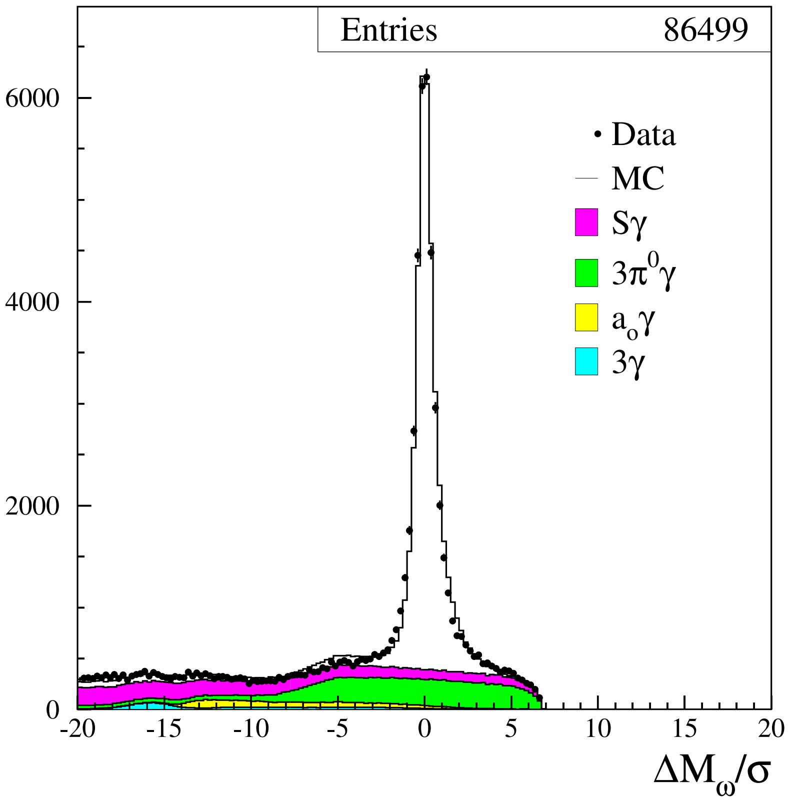

Figure 34: Data-MC comparison for the normalized $\pi^0\gamma$ invariant mass for runs with $\sqrt{s} = 1019.75$ MeV.

samples well reproduces the expected shapes. The agreement is also good for the other center of mass energies. As an example, the $\cos\psi$ distributions are reported in Fig. 36.

The number of events obtained for the different values of $\sqrt{s}$, together with the expected background and the visible cross section, are reported in App. C.

8.2 Fit to the VMD terms

In the energy region below 1.4 GeV, the $\pi^0\pi^0\gamma$ production cross section related to the VMD terms is largely dominated by the not-resonant processes $e^+e^- \to \rho/\rho' \to \omega\pi^0$.

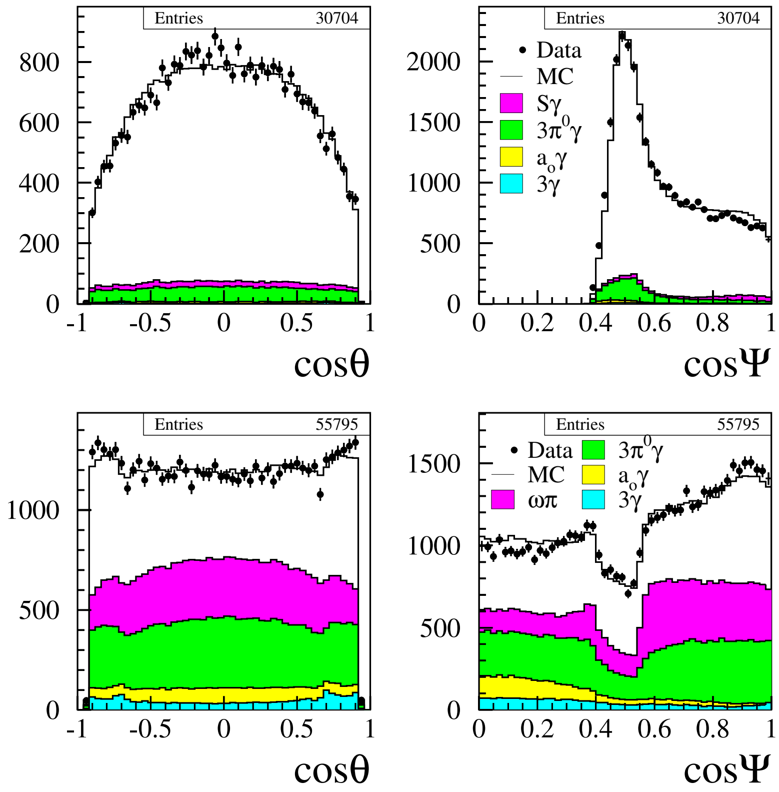

Figure 35: Data-MC comparison for $\omega\pi$ (up) and $S\gamma$ (bottom) events. On the left the polar angle of the primary photon are shown, while on the right there are the distribution of the $\cos\psi$ variable. Only runs with $\sqrt{s} = 1019.75$ MeV are shown.

However, at $\sqrt{s} \sim M_\phi$, sizeable contribution from $\phi \to \rho^0\pi^0$ and from the OZI and G-parity suppressed decay $\phi \to \omega\pi^0$ are expected. The co-existence all of these processes shows up as an interference pattern in the energy dependence of the cross section around the ϕ mass.

The visible cross section is usually written in the form [26]:

$$\sigma^{\omega\pi}(\sqrt{s}) = \sigma_0^{\omega\pi}(\sqrt{s}) \left| 1 - Z\frac{M_\phi \Gamma_\phi}{D_\phi} \right|^2 , \tag{11}$$

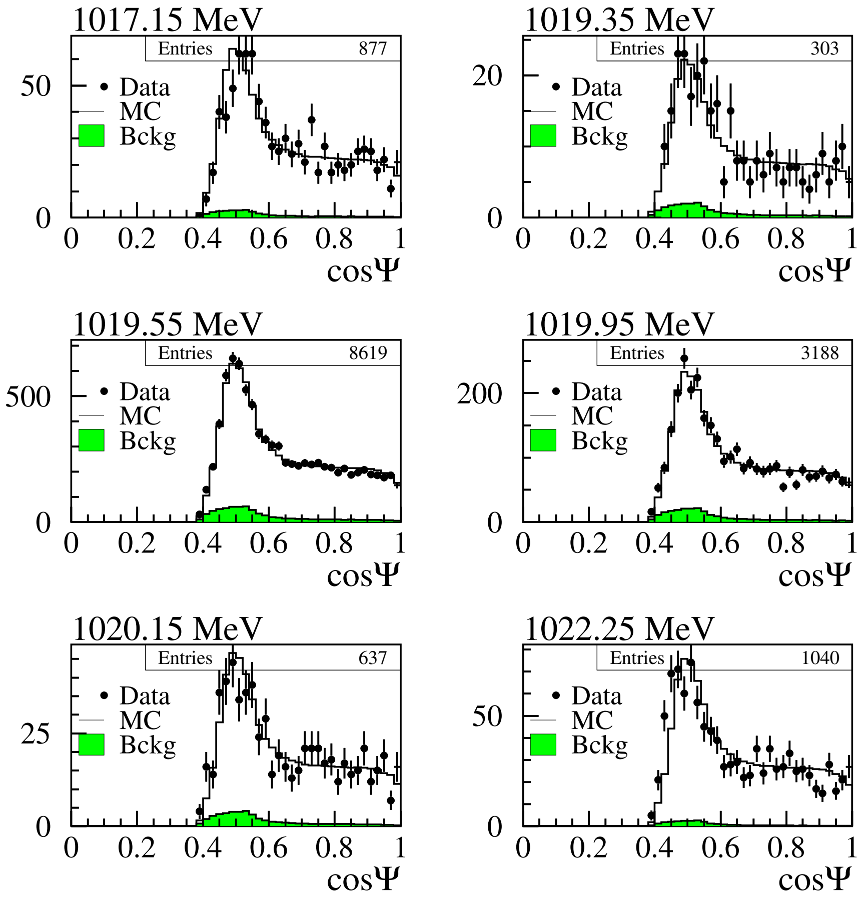

Figure 36: Data-MC comparison for different values of $\sqrt{s}$, specified in the top-left corner of each plot: $\cos\psi$ distributions for $\omega\pi$ events.

where $\sigma_0^{\omega\pi}(\sqrt{s})$ represents the nude cross section for the not-resonant process, Z is the complex interference parameter (i.e. the ratio between the ϕ decay amplitude and the not-resonant process), while M_ϕ , Γ_ϕ and $D_\phi = M_\phi^2 - s - i\sqrt{s}\,\Gamma_\phi$ are respectively the mass, the width and the inverse propagator of the ϕ meson.

The final state $\pi^+\pi^-\pi^0\pi^0$ offers, although with a completely different background composition,[4] a similar description of the interference pattern with the advantage of having only the contribution of the ϕ decay to $\omega\pi^0$. In this case, Z is directly related to the BR of $\phi \to \omega\pi^0$ as follows:

$$\mathrm{BR}(\phi \to \omega\pi^0) = \frac{\sigma_0^{\omega\pi}(M_\phi)|Z|^2}{\sigma_\phi}. \tag{12}$$

A joint measurement of this final state and the $\pi^0\pi^0\gamma$ one will allow the determination of $\mathrm{BR}(\omega \to \pi^0\gamma)$ and a test of the theoretical expectations on the $\phi \to \rho^0\pi^0$ contribution. A description of the existing measurement on these channels and of the KLOE plans to complete this job can be found in Refs. [26, 27, 28].

Let's go back now on the $\pi^0\pi^0\gamma$ final state. To extract the different components we have first to parametrize the $\sqrt{s}$ dependence of the not-resonant born cross section. We did this in three different way:

- (A) Linear dependence: $\sigma_0^{\omega\pi}(\sqrt{s}) = \sigma_0^{\omega\pi} + \sigma'(\sqrt{s} - M_\phi)$. This parametrization is model independent and allows to compare with theoretical prediction as shown in ref. [29]. The only disadvantage is that the slope σ' is an important parameter of the fit and a long lever arm in $\sqrt{s}$ is needed to reliably determine it. As we will see, our existing data set is not enough to determine this parameter and we should fix it to the values obtained from other measurements.

- A model description of the not-resonant cross-section as the sum of ρ and ρ' intermediate states. In this case, $\sigma_0^{\omega\pi}(\sqrt{s})$ is parametrized as follows:

$$\sigma_0^{\omega\pi}(\sqrt{s}) = \frac{K}{s^{3/2}} \left| \frac{M_\rho^2}{D(\rho)} + \frac{A_1 M_{\rho'}^2}{D(\rho')} \right|^2 P_f(\sqrt{s}), \tag{13}$$

  where $A_1 = (\frac{g_{\rho'\omega\pi}}{f_{\rho'}})(\frac{f_\rho}{g_{\rho\omega\pi}})$ is a negative real number equal to the ratio of the coupling constants of ρ and ρ' vector mesons while $D(V) = M_V^2 - s - i\sqrt{s}\,\Gamma_V(\sqrt{s})$ is their inverse propagator. $P_f(\sqrt{s})$ is the phase volume of the final state. To compare with Ref. [26], we used the two different sets of parametrization proposed in their work:

  - (B) $M_{\rho'} = 1465$ MeV and $\Gamma_{\rho'} = 310$ MeV, with the following energy dependence of the ρ-width: $\Gamma_\rho(\sqrt{s}) = \Gamma_\rho(M_\rho)(M_\rho/\sqrt{s})[P_\pi(\sqrt{s})/P_\pi(M_\rho)]^3$, where P_π is the pion momentum;

[4] For this sample, the major background is due to the ϕ decay to $K_S K_L$, with kaons decaying to pion pairs.

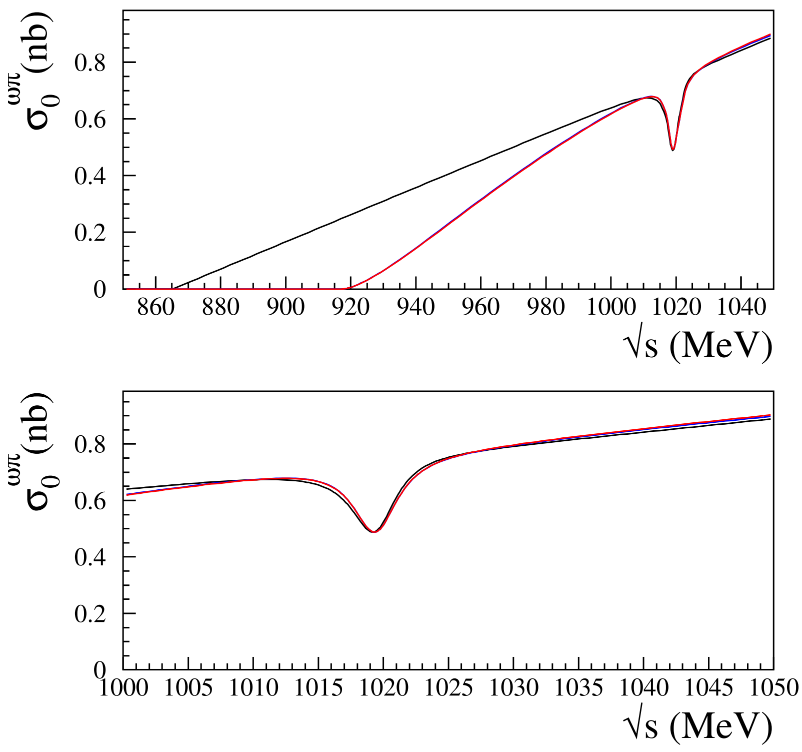

Figure 37: $\sqrt{s}$ dependence of the Born cross section for the VMD terms of the $e^+e^- \to \pi^0\pi^0\gamma$ process: from the threshold to 1050 MeV (top) and a 50 MeV region around M_ϕ bottom. The black, blue and red lines represent parametrization (A), (B) and (C) respectively. Blue and red curves completely overlap.

- (C) $M_{\rho'} = 1530$ MeV and $\Gamma_{\rho'} = 430$ MeV, with the energy dependences of Γ_ρ neglected.

For all of these fits we have therefore at least three free fit parameters, σ_0, $\Re(Z)$ and $\Im(Z)$ while the slope, σ' or A_1, is either fixed or added as additional free parameter. The $\sqrt{s}$-dependence for the three different parametrization of the nude cross sections are reported in Fig. 37. The right threshold behaviour at low energies is respected only by models (B) and (C), that show in addition a very similar shape.

FIT (A)	σ_0 (nb)	$\Re(Z)$	$\Im(Z)$	σ'(nb/MeV)	χ^2/ Ndof
σ' fixed	0.732 ± 0.026	0.049 ± 0.020	-0.164 ± 0.024	0.0045	5.2/11
σ' fixed	0.749 ± 0.027	0.039 ± 0.019	-0.159 ± 0.024	0.0073	5.0/11
FIT (B)	σ_0 (nb)	$\Re(Z)$	$\Im(Z)$	A_1	χ^2/ Ndof
A_1 fixed	0.747 ± 0.024	0.041 ± 0.022	-0.160 ± 0.020	-0.114	5.2/11
A_1 fixed	0.748 ± 0.028	0.040 ± 0.020	-0.159 ± 0.022	-0.150	5.2/11
All free	0.746 ± 0.002	0.042 ± 0.022	-0.160 ± 0.008	-0.063 ± 0.105	5.3/10
FIT (C)	σ_0 (nb)	$\Re(Z)$	$\Im(Z)$	A_1	χ^2/ Ndof
A_1 fixed	0.747 ± 0.029	0.041 ± 0.020	-0.160 ± 0.022	-0.114	5.3/11
A_1 fixed	0.747 ± 0.028	0.040 ± 0.020	-0.160 ± 0.022	-0.150	5.2/11
All free	0.746 ± 0.054	0.043 ± 0.040	-0.161 ± 0.062	-0.050 ± 0.070	5.3/10

Table 8: Results of the fit to the not-resonant $\pi^0\pi^0\gamma$ visible cross section for the three different parametrizations of $\sigma_0^{\omega\pi}(\sqrt{s})$ used. The parameters σ' and A_1 are fixed to the values obtained in Refs. [29, 32, 26].

The values obtained for the $\omega\pi$ visible cross section, listed in App. C, are fit with all the three models. The errors include statistics, background subtraction and systematics of Tab. 7 with a 0.6% due to luminosity added in quadrature. The fit to the visible cross section has been performed after correcting the born cross section for the initial state radiation as follows: $\sigma_{\rm vis}^{\omega\pi}(\sqrt{s}) = \int_{\rm thr}^{\sqrt{s}} \sigma_0^{\omega\pi}(x)\, H_{\rm RAD}(x,\sqrt{s})\, dx$, where $H_{\rm RAD}$ is the radiator function [30] which expresses the probability that ISR photons are emitted from the e^+e^- pair thus lowering the beam energy from $\sqrt{s}$ to x. We have also performed a convolution of the cross section with the beam energy spread, BES, which we have assumed to be in average $\sim$ 300 keV [31]. We have then fit $\sigma_{\rm vis}^{\omega\pi}(\sqrt{s})$ with the three available parametrizations by letting all free the four parameters or fixing the slopes to SND measurements [26]. The results are reported in Tab. 8 and shown in Fig. 38. For case (A) the fit with the free slope does not converge, therefore was not included in the table. Indeed, also for fits (B) and (C) when leaving the slope free its value is evaluated with a huge uncertainty. This is due to the limited range of $\sqrt{s}$ we have in 2001-2002 data. Anyhow, the results are stable even when changing the slopes of a large amount.

To quote final numbers we get the central values from model (C), A_1 fixed to -0.150,

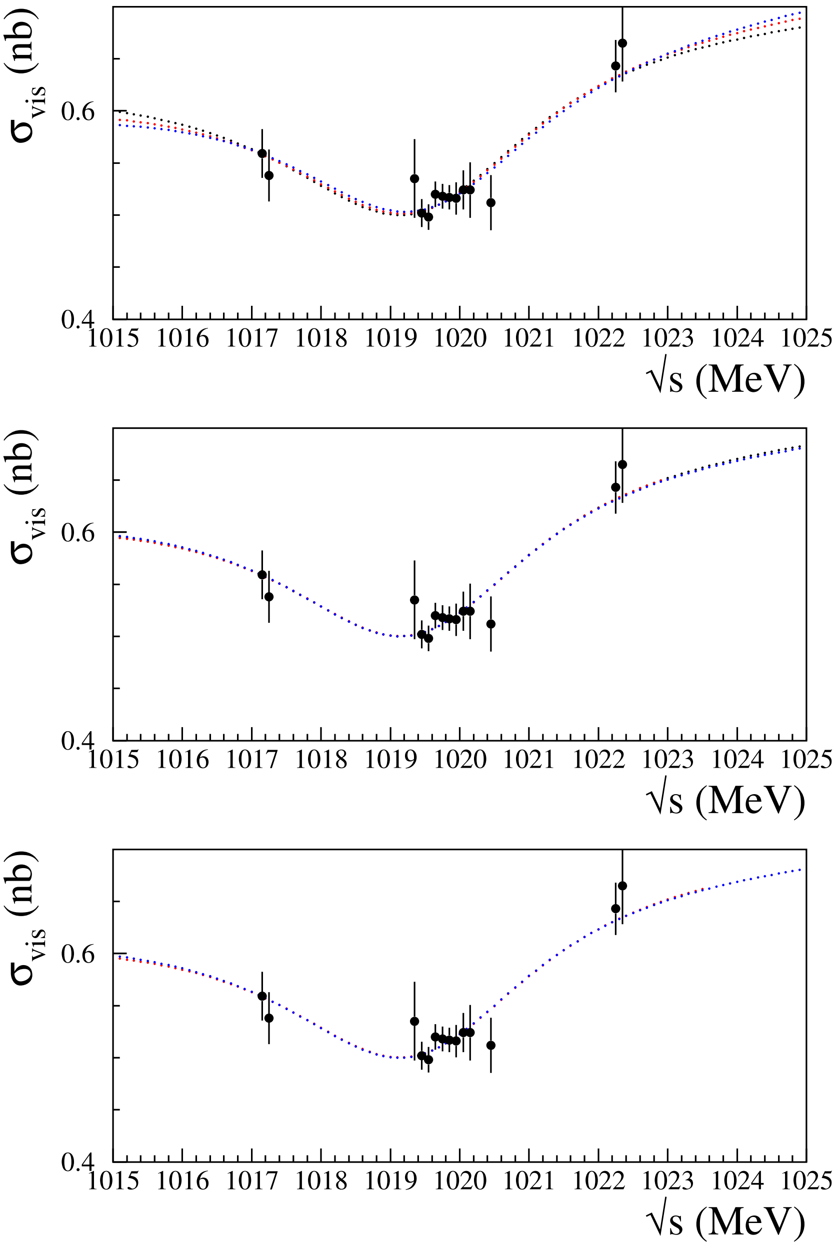

Figure 38: Fit to the $\omega\pi$ visible cross section: black dots are data while dotted lines represents fit results for model (A) [top], (B) [middle] and (C) [bottom]. Black, red and blue lines are the first, second and third fit of Tab. 8 respectively.

M_{f_0}	989 MeV
$g_{f_0\pi^+\pi^-}$	-2.08 (GeV^{-1})
$g_{f_0K^+K^-}$	4.40 (GeV^{-1})
$\Gamma_{\phi K^+K^-}$	2.096 MeV

Table 9: Parameters used to describe the $\phi \to f_0(980)\gamma \to \pi^0\pi^0\gamma$ decay in the kaon loop approach.

while using the maximum excursion of the values as a systematic error. We get:

$$\begin{aligned} \sigma_0^{\omega\pi} &= (\,0.747 \pm 0.028_{\,\mathrm{fit}}\,{}^{+0.001}_{-0.015}{}_{\,\mathrm{syst}}\,)\ \mathrm{nb} && (14)\\ \Re(Z) &= 0.040 \pm 0.020_{\,\mathrm{fit}}\,{}^{+0.009}_{-0.001}{}_{\,\mathrm{syst}} && (15)\\ \Im(Z) &= -0.160 \pm 0.022_{\,\mathrm{fit}}\,{}^{+0.001}_{-0.004}{}_{\,\mathrm{syst}} && (16) \end{aligned}$$

in good agreement and with similar accuracy with respect to SND results [26]: $\sigma_0^{\omega\pi} = (\,0.74 \pm 0.02_{\mathrm{stat}} \pm 0.04_{\mathrm{syst}}\,)$ nb, $\Re(Z) = 0.025 \pm 0.035$, $\Im(Z) = -0.19 \pm 0.05$.

8.3 Fit to the scalar term

The resonant $\pi^0\pi^0\gamma$ cross section part is assumed to be dominated by a scalar meson production of the form $\phi \to S\gamma$ which proceeds through a kaon loop [33]. Under this assumption, we can express the born cross section as:

$$\sigma_0^{S\gamma}(s) = 12\,\pi\,\Gamma_\phi^{e^+e^-}\,\Gamma_\phi^{S\gamma}\left|\frac{1}{D_\phi(s)}\right|^2\left(\frac{M_\phi}{\sqrt{s}}\right)^3 R_\Gamma(s)\,, \tag{17}$$

where $D_\phi = M_\phi^2 - s - i\,\sqrt{s}\,\Gamma_\phi(s)$ is the inverse propagator of the ϕ meson and the $\sqrt{s}$ dependence of Γ_ϕ is dominated by the one of the four main ϕ BRs. The ratio $R_\Gamma(s) = \Gamma_\phi^{S\gamma}(\sqrt{s})/\Gamma_\phi^{S\gamma}(M_\phi)$ contains the energy dependence of $\Gamma_\phi^{S\gamma}$ which is less trivial than for other processes. In order to determine it, we have integrated the differential energy spectrum $d\Gamma/dE_\gamma$, parametrized as in Ref. [33], from threshold to $\sqrt{s}$. We follow the prescription of the kaon loop model in the case of a single scalar meson production, the $f_0(980)$, using the parameters listed in Tab. 9 For the BR($\phi \to e^+e^-$) we use the KLOE measurement $\Gamma_\phi^{ll} = (1.320 \pm 0.017_{\mathrm{stat}} \pm 0.015_{\mathrm{syst}})$ keV [34].

We wrote the born cross section as a function of three parameters: α as a free normalization scale of $\Gamma_{S\gamma}^\phi$, M_ϕ and Γ_ϕ. As in the previous sub-section, the visible cross section is

FIT	α	M_ϕ (MeV)	Γ_ϕ (MeV)	χ^2/ Ndof
(A) All free	1.400 ± 0.012	1019.53 ± 0.08	4.577 ± 0.002	14.7/11
(B) Γ_ϕ fixed	1.389 ± 0.006	1019.35 ± 0.05	4.36	17.2/12
(C) M_ϕ, Γ_ϕ fixed	1.342 ± 0.017	1019.46	4.26	19.8/13

Table 10: Results of the fit to the resonant $\pi^0\pi^0\gamma$ visible cross section for the three different options.

estimated after performing a convolution with the radiator function and the beam energy spread. We made the fit in three different options:

(A) all three parameters free, with the only constraint of bounding M_ϕ and Γ_ϕ in the regions (1019.2−1019.6) MeV and (4.2−4.6) MeV respectively;

(B) fixing Γ_ϕ to the values of 4.36 MeV, found when fitting the line shape of $\phi \to \eta\gamma \to 3\pi^0\gamma$ (see App. A);

(C) fixing M_ϕ and Γ_ϕ to the PDG values (1019.46 MeV and 4.26 MeV respectively).

The results of all these fits are statistically consistent as shown in Tab. 10 although the best fit is obtained when leaving all parameters free and the ϕ-width increases to 4.6 MeV. The behaviour of the cross section nicely agrees with data in the region around M_ϕ as shown in Fig. 39. The only evident deviation is in the tails where data seems to ask for a positive scalar-VMD interference.

From the values of α we determine the width of $\phi \to \pi^0\pi^0\gamma$ at M_ϕ, which is proportional to $(g_{f_0 K^+K^-} \times g_{f_0 \pi^+\pi^-})^2$: $\Gamma(\phi \to \pi^0\pi^0\gamma) = (\,0.436 \pm 0.006_{\rm stat} \pm 0.019_{\rm syst}\,)$ keV. We use for the central value the results from fit (C) and for the systematic error the maximum excursion of $\Gamma(\phi \to \pi^0\pi^0\gamma)$ obtained with the three different fits. When dividing by $\Gamma_\phi(M_\phi)$, we determine the branching fraction of the $\phi \to \pi^0\pi^0\gamma$ process to be:

$$\mathrm{BR}(\phi \to \pi^0\pi^0\gamma) = (\,1.023 \pm 0.013_{\,\rm fit}\ {}^{+0.028}_{-0.010\,\rm norm}\,) \cdot 10^{-4}\,. \tag{18}$$

The result is in pretty good agreement with our old measurement [6].

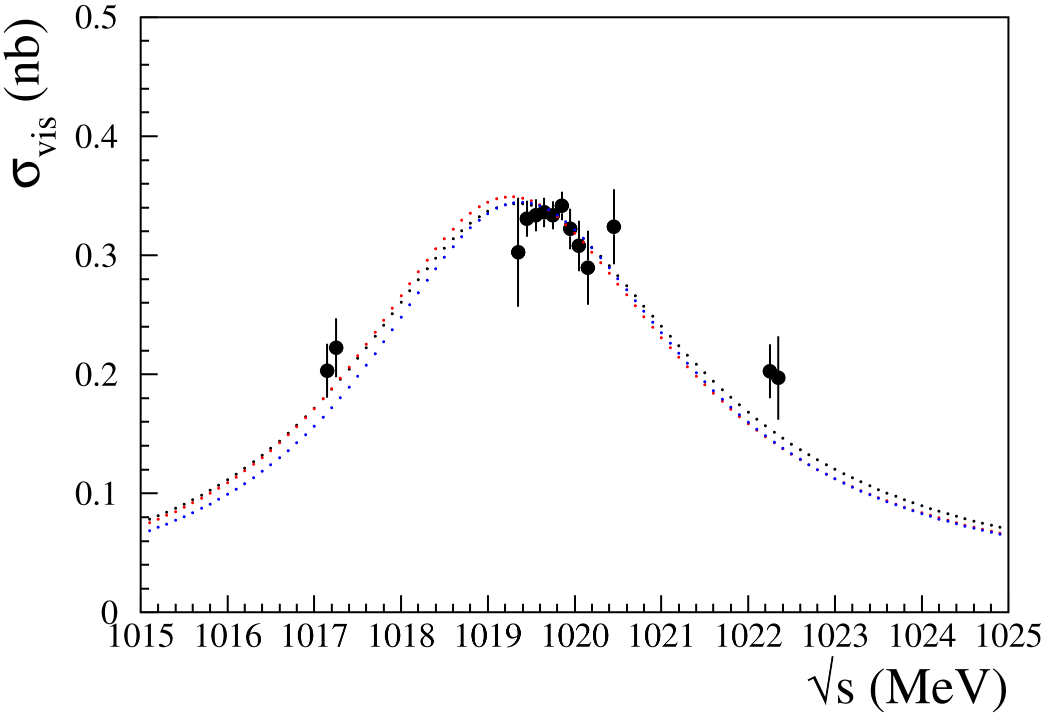

Figure 39: Fit to the resonant $\pi^0\pi^0\gamma$ visible cross-section. Black dots are data while dotted lines represents fit results: black, blue and red lines are fit (A), (B) and (C) respectively.

9 Conclusions

As stated in the introduction, we have determined the visible cross section for the process $e^+e^- \to \pi^0\pi^0\gamma$ in the energy region $1017.0 < \sqrt{s} < 1022.2$ MeV. No attempt has been made in fitting the $M_{\pi\pi}$ spectrum or the Dalitz plot. We have simply subdivided the events in two categories depending on the reconstructed value of $M_{\pi\gamma}$. The $e^+e^- \to \omega\pi^0$ process seems to be very well described by this separation and dominates the region with $M_{\pi\gamma}$ around M_ω. Data clearly show also its not resonance behaviour and the interference with the ϕ meson. This process shows also a clear indication of spin 1 angular dependence in its decay which well matches the Montecarlo expectations. The remnant of the events are reasonably described by a resonant behaviour of an intermediate scalar term which however is not fully described by our Montecarlo. We leave the questions to be settled down by a fit to the Dalitz plot in a forthcoming note.

Acknowledgements

We want to thank many people which helped us in understanding these processes and in focusing our analysis towards a more solid conclusion. In particular, we are in debt with N. N. Achasov and A. V. Kiselev to have shown in a continuous way how to proper treat the theoretical problems hidden in various point. Moreover, we cannot forget G. Isidori, L. Maiani and S. Pacetti to have test most of the cross-section we use in the generators and be always friendly with us. We have also to thank P. Gauzzi for the joint-development of the $e^+e^- \to \omega\pi^0$ generator, M. Palutan and T. Spadaro for giving us the new photon efficiency curves, M. Dreucci and M. Antonelli for the ISR generator.

A $\phi \to \eta\gamma$ line shape

To calibrate our largest background source and to test our normalization procedure with a much larger cross-section we have also determined the visible cross section for the process $\phi \to \eta\gamma$ with $\eta \to \pi^0\pi^0\pi^0$. We closely follow what is done for the final state with five photons. After requiring a calorimeter trigger and the event classification filter to be satisfied, we have selected events with seven prompt photons. The selection of photons requires the clusters to be in the expected time window (TW), to have energy above 7 MeV and to be produced in a polar angle with $23^\circ < \theta_\gamma < 157^\circ$. In order to select the radiative photon, the most energetic cluster in the event should have an energy above 280 MeV. We also require a cut on missing momentum and total energy to reduce to a negligible amount the $\phi \to K_S K_L$ background, retaining only events with $P_{\rm miss} < 200$ MeV and $E_{\rm tot} > 700$ MeV. A prescaling factor of 50 has been applied when selecting the events. To extract the visible cross section we finally correct for the efficiency of the acceptance selection and for the integrated luminosity used.

To control the systematics related to the exclusive photon counting, we have streamed a sub-sample of data requiring a much looser selection. We required from 6 to 8 photons in TW with an angular acceptance $18^\circ < \theta_\gamma < 162^\circ$. We have done three tests to access the systematic variation on the cross-section.

1. The old and new efficiency curves (see Par. 7.2) have been applied to the MC. The acceptance of seven exclusive photons varies from 0.394 to 0.402 which corresponds to a systematic change of $\sim 2\%$.

2. The angular and energy selection for the clusters have been hardened to 30° and 20 MeV respectively. While these requests dramatically reduce the acceptance from 0.402 to 0.230, the estimated cross-section changes only of $+1.2\%$.

3. As a final test, we also compare the inclusive and exclusive determination of the cross-section by counting all events with 6, 7 and 8 photons in the control sub-sample. The estimated cross-section varies of -3.3%.

In the following, we assign 3.3% as the dominant systematic error related to this cross section measurement.

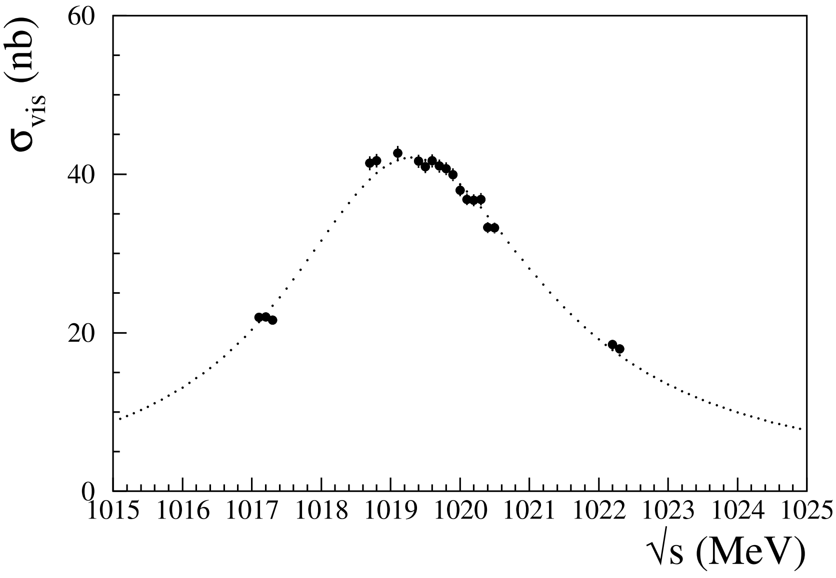

Figure 40: $\sqrt{s}$-dependence of the $\phi \to \eta\gamma$ cross-section. Black points are data, dotted line is the fit result.

The born cross section $\sigma_0^{\eta\gamma}$ is written as follows:

$$\sigma_0^{\eta\gamma} = 12\,\pi\,\Gamma_\phi^{e^+e^-}\,\Gamma_\phi^{\eta\gamma}\left|\frac{e^{i\pi}}{D_\phi} + \frac{R_\rho}{D_\rho} + \frac{R_\omega}{D_\omega}\right|^2 \left(\frac{M_\phi}{\sqrt{s}}\right)^3 \left(\frac{Q_\eta(\,\sqrt{s}\,)}{Q_\eta(\,M_\phi)}\right)^3\,, \tag{19}$$

where $D_V = M_V^2 - s - i\,\sqrt{s}\,\Gamma_V(s)$ are the inverse propagators of ϕ, ρ and ω mesons and Q_η is the η-momentum in the ϕ rest-frame. The ratios R_V between the propagators are defined as $R_V = \sqrt{\frac{W_V}{W_\phi}}$ where W_V is

$$W_V = \Gamma_V^2\;M_V^3\;\mathrm{BR}(V \to e^+e^-)\;\mathrm{BR}(V \to \eta\gamma)\;Q_\eta(M_V)\,. \tag{20}$$

The fit to the visible cross section is done after convoluting with the radiator and the beam energy spread. For $\Gamma_\phi^{e^+e^-}$ we use the KLOE measurement $\Gamma_\phi^{ll} = (1.320 \pm 0.017_{\mathrm{stat}} \pm 0.015_{\mathrm{syst}})$ keV. We left three free parameters on the fit: a normalization factor for the product of the branching ratios $\mathrm{BR}(\phi \to \eta\gamma)\cdot\mathrm{BR}(\eta \to 3\pi^0)$, α, and the ϕ mass and width. The difference of α from unity represents our miscalibration of the absolute scale. The fit nicely reproduces the data as shown in Fig. 40. The χ^2/Ndof of the fit is of 16.8/17 and the extracted parameters are:

$$\alpha = 1.014 \pm 0.010 \tag{21}$$

$$M_\phi = (\,1019.41 \pm 0.01\,)\ \text{MeV} \tag{22}$$

$$\Gamma_\phi = (\,4.36 \pm 0.09\,)\ \text{MeV} \tag{23}$$

The value of BR($\phi \to \eta\gamma$) is still statistically consistent with the PDG measurement. Similar conclusion can be drawn for the M_ϕ and Γ_ϕ values. This last result enforced our belief of a good calibration of the center of mass energy scale and of our absolute normalization.

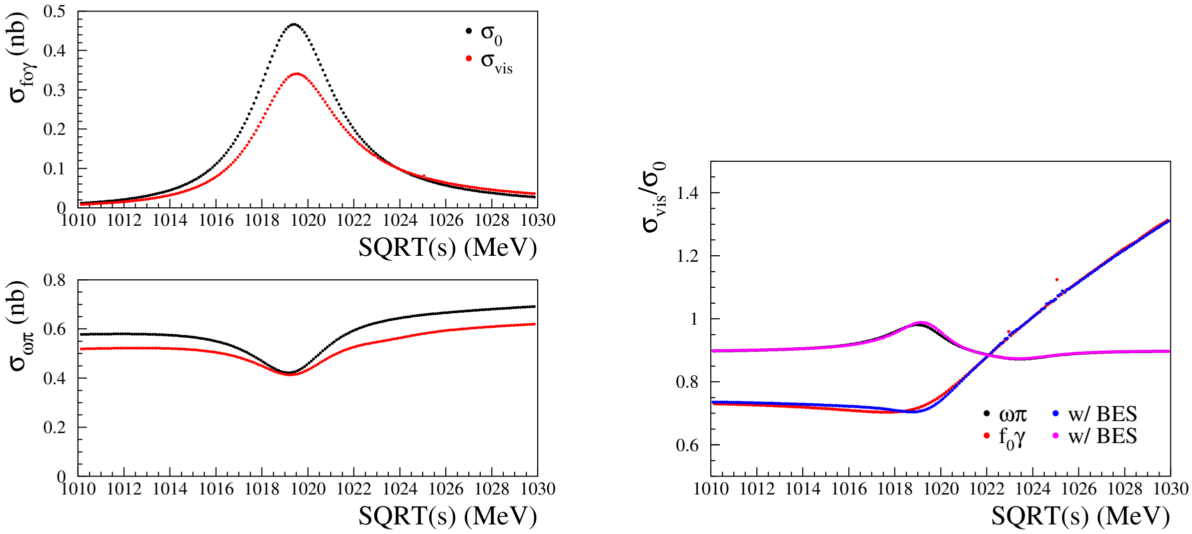

Figure 41: Left panel: nude (black) and visible (red) cross section as a function of $\sqrt{s}$ for $S\gamma$ (top) and $\omega\pi$ (bottom) processes. The ratio between $\sigma_{\rm vis}$ and σ_0 is reported in the right panel either taking into account or neglecting the effect of the beam energy spread.

B Radiative corrections related to Initial State Radiation

To understand the corrections due to the initial state radiation, we have convoluted the nude cross section (σ_0) with the standard generation of initial state radiation [30] in a standalone program. For the theoretical description of $\omega\pi$ and $S\gamma$ processes we have used the paramatrization of section 8.2 – model(C) – and 8.3 respectively. in Fig. 41.left both the nude and the visible cross sections are shown for the two processes. The ratio between the two is reported in Fig. 41.right, and represents the average correction due to ISR as a function of $\sqrt{s}$. As expected, the two curves are very different due to the resonant and continuum behaviour of the two processes.

Using our standalone ISR generator, we have checked the energy distribution of the ISR photons produced by GEANFI. As shown in Fig. 42, there are same discrepancies in the description of the tails. This is not a problem for $S\gamma$ events where, due to the resonant behaviour of the process, the $E_{\rm ISR}$ distribution has a cutoff at 20 MeV. On the other hand, the ISR tails of $\omega\pi$ events are much more extended to higher energy values. Since during

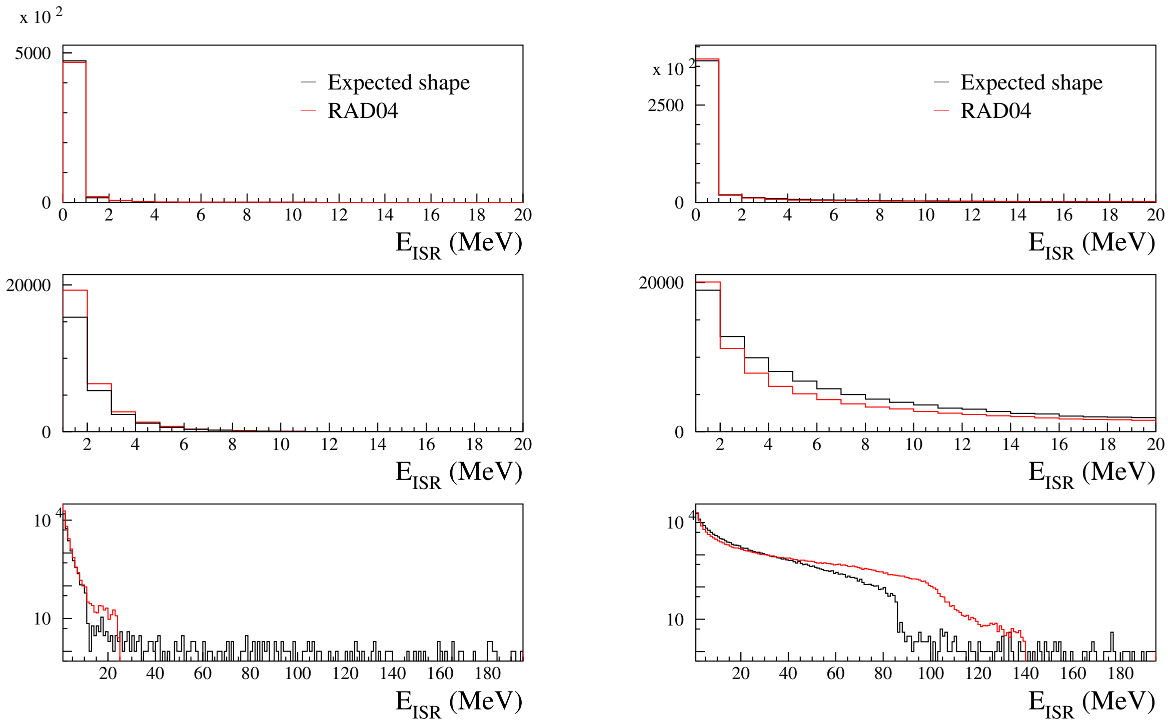

Figure 42: Energy emitted from the initial state radiation for $S\gamma$ (left) and $\omega\pi$ (right) processes, for different $E_{\rm ISR}$ ranges. The ISR tails from GEANFI are reported in red, while the output of the standalone generator is shown in black.

the kinematic fit we constraint the total energy of the event to the nominal $\sqrt{s}$ value with an error of 300 keV due to BES, a variation on $E_{\rm ISR}$ tails modifies the shape of $\chi^2_{\rm Fit2}$. A tight cut on this variable thus produces a wrong determination of the analysis efficiency. In order to reduce this effect we have:

1. reproduced in $\omega\pi$ MC the tail of the standalone generator for $E_{\rm ISR}$ using an hit-or-miss procedure;

2. used a mild cut on the χ^2 of the kinematic fit: $\chi^2_{\rm Fit2}/{\rm ndf} < 5$.

In Fig. 43 the variation of the analysis efficiency for $\omega\pi$ events using the two ISR energy distributions is reported. While the effect is flat in $M_{\pi\pi}$, the $M_{\pi\gamma}$ projection of the Dalitz plot shows that the effect is concentrated in the region 620–760 MeV. This is related to

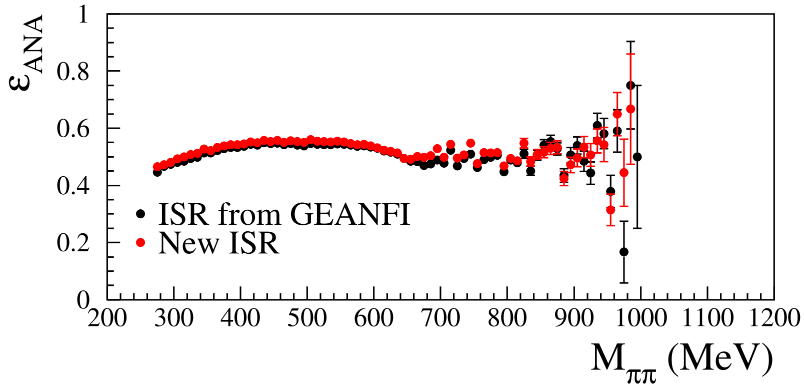

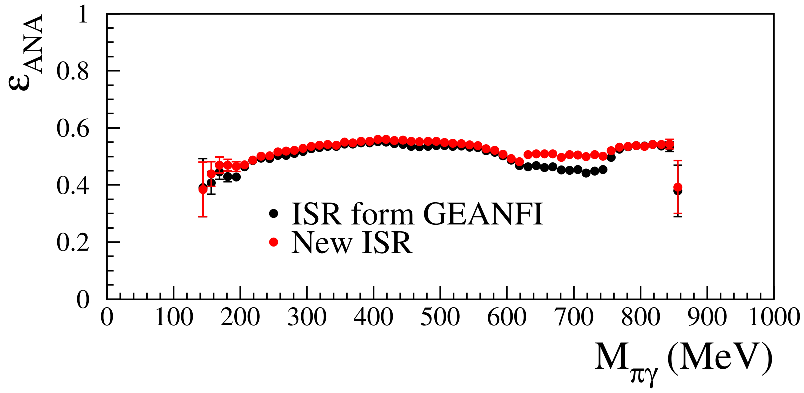

Figure 43: Analysis efficiency for $\omega\pi$ MC events in the two projections of the Dalitz plot after the $\chi^2_{\rm Fit2} < 5$ cut. In black the ISR inserted in GEANFI is used, while in red the new ISR parametrization is applied.

the events with higher ISR energy which are concentrated on the left tail of the two $M_{\pi\gamma}$ peaks (see Fig. 44).

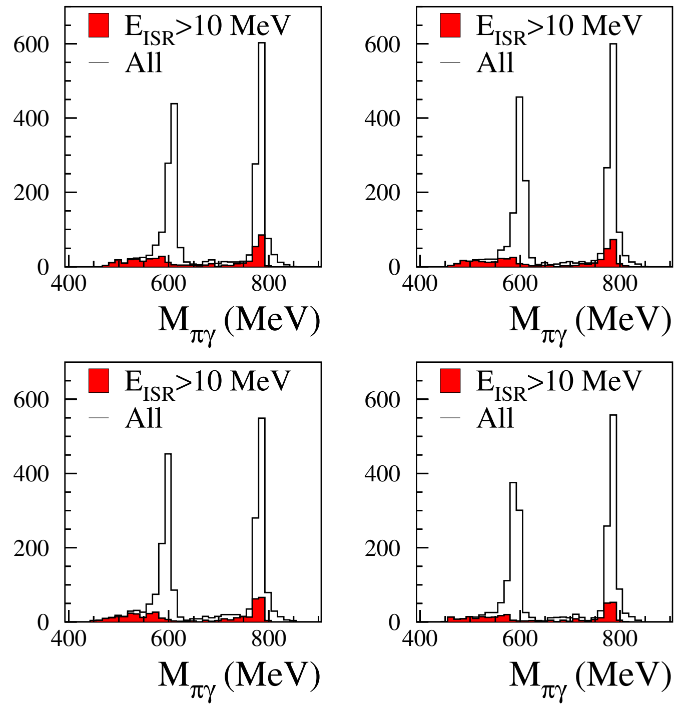

Figure 44: $M_{\pi\gamma}$ distributions for $\omega\pi$ MC events for different slices of the Dalitz plot: $M_{\pi\pi}$= 305 MeV (top-left), $M_{\pi\pi}$= 315 MeV (top-right), $M_{\pi\pi}$= 325 MeV (bottom-left) and $M_{\pi\pi}$= 335 MeV (bottom-right). In black the complete distribution is shown, while in red only the events with $E_{\mathrm{ISR}} > 10$ MeV are displayed.

C Tables of cross sections for the $\pi^0\pi^0\gamma$ final state

1. $\phi \to S\gamma \to \pi^0\pi^0\gamma$

$\sqrt{s}$ (MeV)	N	B	N–B	$\sigma_{S\gamma}$ (nb)
1017.15	1050 ± 32	649.2 ± 15.5	400.8 ± 44.1	0.203 ± 0.023
1017.25	925 ± 30	551.7 ± 14.4	373.3 ± 41.0	0.222 ± 0.025
1019.35	521 ± 23	316.0 ± 10.0	205.0 ± 30.6	0.303 ± 0.046
1019.45	10221 ± 101	5919.4 ± 114.3	4301.6 ± 170.9	0.331 ± 0.015
1019.55	16155 ± 127	9311.1 ± 176.5	6843.9 ± 238.0	0.334 ± 0.014
1019.65	30003 ± 173	17325.0 ± 319.6	12678.0 ± 386.6	0.336 ± 0.012
1019.75	55795 ± 236	32220.1 ± 589.5	23574.9 ± 660.0	0.334 ± 0.012
1019.85	42622 ± 206	24263.5 ± 442.0	18358.5 ± 512.1	0.341 ± 0.012
1019.95	5680 ± 75	3300.6 ± 65.1	2379.4 ± 115.0	0.322 ± 0.017
1020.05	2815 ± 53	1663.1 ± 34.9	1151.9 ± 75.5	0.308 ± 0.021
1020.15	1066 ± 33	641.9 ± 16.3	424.1 ± 44.4	0.290 ± 0.031
1020.45	1037 ± 32	582.0 ± 15.1	455.0 ± 43.0	0.324 ± 0.032
1022.25	1116 ± 33	699.2 ± 16.4	416.8 ± 45.6	0.203 ± 0.023
1022.35	447 ± 21	283.8 ± 9.9	163.2 ± 28.8	0.197 ± 0.035

Table 11: Summary table for $S\gamma$ events as a function of $\sqrt{s}$: number of events (N), expected background (B) and their difference (N–B). The errors on the last two quantities include the MC statistics and the systematics on the background evaluation. In the last column, the visible cross sections are listed. Also here the error includes just the statistics and the background evaluation; a further relative error of 2.15% due to systematics have to be added in quadrature to have the whole error on $\sigma_{S\gamma}$.

2. $e^+e^- \to \omega\pi^0 \to \pi^0\pi^0\gamma$

$\sqrt{s}$ (MeV)	N	B	N–B	$\sigma_{\omega\pi}$ (nb)
1017.15	877 ± 30	46.2 ± 1.8	830.8 ± 30.4	0.559 ± 0.020
1017.25	722 ± 27	41.7 ± 1.6	680.3 ± 27.7	0.538 ± 0.022
1019.35	303 ± 17	29.9 ± 1.2	273.1 ± 18.3	0.535 ± 0.036
1019.45	5497 ± 74	585.7 ± 14.5	4911.3 ± 79.3	0.502 ± 0.008
1019.55	8619 ± 93	925.7 ± 22.5	7693.3 ± 100.3	0.498 ± 0.006
1019.65	16483 ± 128	1694.8 ± 40.5	14788.3 ± 140.8	0.520 ± 0.005
1019.75	30704 ± 175	3147.9 ± 74.8	27556.1 ± 198.6	0.518 ± 0.004
1019.85	23307 ± 153	2380.4 ± 56.1	20926.6 ± 169.8	0.517 ± 0.004
1019.95	3188 ± 56	318.6 ± 8.2	2869.4 ± 59.8	0.516 ± 0.011
1020.05	1632 ± 40	157.5 ± 4.4	1474.5 ± 42.5	0.524 ± 0.015
1020.15	637 ± 25	59.6 ± 2.0	577.4 ± 26.5	0.524 ± 0.024
1020.45	597 ± 24	55.4 ± 1.9	541.6 ± 25.6	0.512 ± 0.024
1022.25	1040 ± 32	43.6 ± 1.8	996.4 ± 33.0	0.643 ± 0.021
1022.35	432 ± 21	16.9 ± 1.0	415.1 ± 21.2	0.665 ± 0.034

Table 12: Summary table for $\omega\pi$ events as a function of $\sqrt{s}$: number of events (N), expected background (B) and their difference (N–B). The errors on the last two quantities include the MC statistics and the systematics on the background evaluation. In the last column, the visible cross sections are listed. Also here the error includes just the statistics and the background evaluation; a further relative error of 2.15% due to systematics have to be added in quadrature to have the whole error on $\sigma_{\omega\pi}$.

References

[1] N. A. Törnqvist, Phys. Rev. Lett. 49 (1982) 624.

[2] R. L. Jaffe, Phys. Rev. D 15 (1997) 267.

[3] J. Weinstein and N. Isgur, Phys. Rev. Lett. 48 (1982) 659.

[4] E. M. Aitala *et al.*, Phys. Rev. Lett. 86 (2001) 770.

[5] BES Collaboration, M. Ablikim *et al.*, Phys. Lett. B 598 (2004) 149.

[6] S. Giovannella and S. Miscetti, KLOE Note 178 (2002).

[7] C. Bini, P. Gauzzi, S. Giovannella, D. Leone and S. Miscetti, KLOE Note 173 (2002).

[8] S. Giovannella and S. Miscetti, KLOE Memo 326 (2006).

[9] V. M. Aulchenko *et al.*, Nucl. Phys. B 569 (2000) 158-182.

[10] K. Hagiwara *et al.*, Phys. Rev. D 66 (2002) and 2003 off-year partial update for the 2004 edition available on the PDG WWW pages (*http://pdg.lbl.gov/*)

[11] F. Ambrosino *et al.*, Nucl. Instr. and Meth. A 534 (2004) 403-433.

[12] M. Antonelli and M. Dreucci, KLOE Note 181 (2002).

[13] M. Martini and S. Miscetti, KLOE Note 201 (2005).

[14] F. Bossi, M. Moulson, M. Palutan and B. Sciascia, KLOE Memo 281 (2003).

[15] S. Giovannella and S. Miscetti, KLOE Note 177 (2002).

[16] A. Denig and F. Nguyen, KLOE Note 202 (2005).

[17] M. Dreucci *et al.*, 3^{rd} KLOE Physics Workshop, Capri – May 23^{rd}-26^{th} 2003, *http://www.lnf.infn.it/kloe/private/talks/KPW03/KPW03_dreucci.ppt*

[18] P. Gauzzi, 3^{rd} KLOE Physics Workshop, Capri – May 23^{rd}-26^{th} 2003, *http://www.lnf.infn.it/kloe/private/talks/KPW03/KPW03_gauzzi.ppt*

[19] W. T. Eadie *et al.*, "Statistical Methods in Experimental Physics", North-Holland (1971).

[20] S. Giovannella and S. Miscetti, KLOE Memo 244 (2001).

[21] B. Golosio, M. Incagli and G. Venanzoni, KLOE Memo 172 (1998).

[22] C. Di Donato, KLOE Memo 306 (2005).

[23] T. Spadaro, "*Studies of K_S decays at the KLOE Experiment*", Ph.D. thesis, Università degli Studi di Roma "La Sapienza", XIV ciclo, 2001.

[24] M. Martini and S. Miscetti, KLOE Note 200 (2005).

[25] C. Gatti, M. Palutan and T. Spadaro, KLOE Note 209 (2006).

[26] V. M. Aulchenko *et al.*, J. Exp. Th. Phys. 90 (2000) 927-938.

[27] A. De Santis, "Misura della sezione d'urto del processo $e^+e^- \to \omega\pi^0 \to \pi^+\pi^-\pi^0\pi^0$ con il rivelatore KLOE a DAFNE e sua influenza per gli studi di interferometria quantistica con i mesoni K neutri", thesis, Università degli Studi di Roma "La Sapienza", Anno Accademico 2003/2004, unpublished.

[28] F. Ambrosino *et al.*, KLOE Memo 307 (2005).

[29] M. N. Achasov *et al.*, Nucl. Phys. B 486 (2000) 29.

[30] M. Greco *et al.*, Phys. Lett. B 318 (1993) 635.
E. A. Kuraev, V. S. Fadin, Sov. J. Phys. 41 (1985) 466.

[31] *http://www.lnf.infn.it/kloe/private/bes2002.html*

[32] M. N. Achasov *et al.*, Phys. Lett. B 449 (1999) 122.

[33] N. N. Achasov and V. N. Ivanchenko, Nucl. Phys. B 315 (1989) 465.

[34] F. Ambrosino *et al.*, Phys. Lett. B 608 (2005) 199.